The Astrophysical Journal, 1002:82 (29pp), 2026 May 1 https://doi.org/10.3847/1538-4357/ae5056

CLASSY. XIV. The Nitrogen Exception—Multiphase Enrichment and Feedback in High-z Analogs*

Bethan L. James[1], Valentina Abril-Melgarejo[2,3], Karla Z. Arellano-Córdova[4], Adarsh Ranjan[2], Kaelee S. Parker[5,6], Danielle A. Berg[5,6], Matilde Mingozzi[1], Alessandra Aloisi[2,7], John Chisholm[5,6], Timothy Heckman[8], Alaina Henry[2], Svea Hernandez[9], Kristen B. W. McQuinn[2,10], Xinfeng Xu[8], and Chiaki Kobayashi[11]
THE CLASSY COLLABORATION
[1] ESA for AURA Space Telescope Science Institute 3700 San Martin Drive, Baltimore, MD 21218, USA; bjames@stsci.edu
[2] Space Telescope Science Institute, 3700 San Martin Drive, Baltimore, MD 21218, USA
[3] LUX, Observatoire de Paris, Université PSL, CNRS, Sorbonne Université, Meudon, 92190, France
[4] Institute for Astronomy, University of Edinburgh, Royal Observatory, Edinburgh, EH9 3HJ, UK
[5] Department of Astronomy, The University of Texas at Austin, 2515 Speedway, Stop C1400, Austin, TX 78712, USA
[6] Cosmic Frontier Center, The University of Texas at Austin, Austin, TX 78712, USA
[7] Astrophysics Division, Science Mission Directorate, NASA Headquarters, 300 E Street SW, Washington, DC 20546, USA
[8] Center for Astrophysical Sciences, Department of Physics & Astronomy, Johns Hopkins University, Baltimore, MD 21218, USA
[9] ESA for AURA, Space Telescope Science Institute, 3700 San Martin Drive, Baltimore, MD 21218, USA
[10] Rutgers University, Department of Physics and Astronomy, 136 Frelinghuysen Road, Piscataway, NJ 08854, USA
[11] Centre for Astrophysics Research, Department of Physics, Astronomy and Mathematics, University of Hertfordshire, Hatfield, AL10 9AB, UK
Received 2025 November 6; revised 2026 March 5; accepted 2026 March 9; published 2026 April 27

Abstract

We present a first-of-its-kind analysis of the metal content across two interstellar medium (ISM) phases in a sample of 31 local star-forming galaxies from the COS Legacy Archive Spectroscopic SurveY, selected as analogs of high-z systems. Using cospatial UV absorption and optical emission-line spectroscopy, we compare abundances of N, O, S, and Fe in the low-ionization (neutral) and high-ionization (ionized) gas, providing a multiphase view of enrichment shortly after the current starburst and over longer timescales when ejecta from previous episodes have cooled and mixed. We find that O and S, produced predominantly in short-lived massive stars, are well mixed between the two phases, with scatter reflecting local inhomogeneities. Fe, predominantly produced by Type Ia supernovae on ∼1 Gyr timescales, is higher in the neutral gas, reflecting either delayed mixing of older Fe-enriched material or preferential depletion of Fe from the ionized phase through dust formation in core-collapse supernova ejecta. N exhibits the largest phase offset, with N/H_{ion} systematically ∼0.7 dex higher than N/H_{neu}, and the magnitude of this offset correlates with stellar mass, metallicity, star formation rate, and most strongly with the ISM outflow velocity. N/O ratios in the ionized phase rise rapidly within 3–6 Myr relative to the neutral gas, consistent with N enrichment dominated by Wolf–Rayet stars rather than intermediate-mass asymptotic giant branch stars on longer timescales. These results demonstrate that localized stellar feedback, outflows, and phase-dependent mixing collectively regulate the chemical evolution of star-forming galaxies, providing key insight into the extreme N/O abundances recently observed in galaxies at cosmic dawn.

Unified Astronomy Thesaurus concepts: Ultraviolet astronomy (1736); Dwarf galaxies (416); Galaxy chemical evolution (580); Galaxy spectroscopy (2171); High-redshift galaxies (734); Emission line galaxies (459); Chemical abundances (224)

Materials only available in the online version of record: figure set

1. Introduction

Chemical evolution, i.e., the production, distribution, and cycling of elements within galaxies, is a fundamentally four-dimensional problem. Observationally, we know that metallicity varies spatially across galaxies (e.g., L. Searle 1971; D. Zaritsky et al. 1994; D. Mast et al. 2014; B. L. James et al. 2020) and extends beyond them, as metals are ejected into the circumgalactic medium (CGM) and intergalactic medium (IGM). A third dimension arises from the gas phase: metals reside in both cooler ($T \sim 100$ K), neutral gas (H I) and warmer ($T \sim 10^4$ K), ionized gas (H II). The latter is well traced by optical emission lines from gas, while the former can only be probed through UV interstellar absorption lines. These UV diagnostics are crucial for quantifying the metals locked in the colder interstellar medium (ISM)—rather than the recently ejected, ionized material—and for connecting present-day enrichment to the star-forming gas reservoir that fuels future generations of stars (A. Emerick et al. 2020).

Elements are produced and injected into the ISM on different timescales depending on their nucleosynthetic origin, defining the fourth dimension of chemical evolution in a physical sense. α-elements (O, S, Si) are synthesized predominantly in Type II supernovae (SNe) on ∼5–10 Myr

---

[*] The NASA/ESA HST data presented in this article were obtained from the Mikulski Archive for Space Telescopes (MAST) at the Space Telescope Science Institute, which is operated by the Association of Universities for Research in Astronomy, Inc., under NASA contract NAS 5-26555. The specific observations analyzed can be accessed via doi: 10.17909/n40j-sw87.

timescales, whereas C and N arise mainly from asymptotic giant branch (AGB) stars after $\gtrsim$100 Myr, and Fe-peak elements from Type Ia SNe on $\sim$1 Gyr timescales (C. Kobayashi et al. 2006, 2020; F. Matteucci 2012). C and N can also be rapidly released by Wolf–Rayet (W-R) stars within $\sim$5 Myr of a burst (P. A. Crowther 2007), whose strong winds expose and expel N- and C-enriched core material into the surrounding ISM. Stellar abundance patterns in the Milky Way's halo, thick disk, and thin disk provide complementary, time-integrated constraints on chemical evolution across these enrichment timescales (e.g., B. M. Tinsley 1979; F. Matteucci & E. Brocato 1990; B. Edvardsson et al. 1993; A. McWilliam 1997; J. Bland-Hawthorn & O. Gerhard 2016); in contrast, the gas-phase abundances explored here trace ongoing enrichment and mixing in actively star-forming systems.

Within these enrichment cycles, newly produced metals cool, mix, and transition between ionized and neutral phases. The relative abundances in each phase therefore encode the timescale since the most recent burst of star formation. The ionized gas encodes recent, localized enrichment while also retaining contributions from earlier stellar generations, whereas the neutral phase predominantly integrates the long-term chemical history of the system. Comparing these abundance patterns allows us to probe how metals are dispersed and homogenized across galaxies (B. James & A. Aloisi 2018; S. Hernandez et al. 2020; V. Abril-Melgarejo et al. 2024), providing direct constraints on the physical processes that drive chemical evolution.

Elemental abundance ratios—particularly those tracing elements produced on different timescales—act as powerful diagnostics of evolutionary stage. Ratios such as α/Fe and N/O serve as "chemical clocks" distinguishing early, α-enhanced systems from more evolved, N-enriched ones (A. McWilliam 1997; E. Pérez-Montero et al. 2013; D. A. Berg et al. 2019). When measured in multiple phases, these ratios reveal both ongoing and past enrichment episodes: phase-dependent offsets indicate incomplete mixing, while their evolution with stellar age constrains the characteristic timescales over which newly synthesized material disperses through the ISM (V. Abril-Melgarejo et al. 2024).

Simulations suggest that metal mixing in galaxies occurs over $\lesssim$40 Myr to $\sim$0.1–1 Gyr (Y. Hirai & T. R. Saitoh 2017; A. Emerick et al. 2020; M. Arabsalmani et al. 2023, and references therein), depending on galaxy mass, ISM density, feedback energy, and star formation rate (SFR). In low-mass systems, mixing efficiency increases during periods of high SFR, when stronger galactic outflows and enhanced turbulence promote redistribution (A. Emerick et al. 2020; L. C. Hunter et al. 2022). Observationally, metal-enriched outflows are a dominant factor shaping the distribution of metals, with outflow metallicities often 10–50 times higher than the ISM (J. Chisholm et al. 2018). Low-mass galaxies, in particular, retain metals inefficiently (K. B. W. McQuinn et al. 2015), and a substantial fraction of their metals are found in the CGM or IGM (Y. Zheng et al. 2024). Conversely, localized conditions can delay mixing: strong density contrasts or turbulent mixing layers can trap newly ejected metals in confined regions, leading to highly localized N enrichment as seen in NGC 5253 and Mrk 996 (B. L. James et al. 2009; M. S. Westmoquette et al. 2013; N. Kumari et al. 2018).

Despite their importance, direct multiphase abundance comparisons remain rare because UV absorption studies require high-signal-to-noise ratio (S/N) spectroscopy from space-based observatories. To date, only a few systems have been examined in this way. In some, the neutral and ionized-gas metallicities agree within uncertainties (V. Lebouteiller et al. 2009; B. James & A. Aloisi 2018; S. Hernandez et al. 2021), while in others, significant phase offsets are found. In the spatially resolved study of NGC 5253 by V. Abril-Melgarejo et al. (2024), N/H and O/H in the neutral gas were lower than in the ionized gas by 0.8 and 0.22 dex, respectively. By comparing clusters of different ages, they inferred a $\sim$10–15 Myr mixing timescale between phases—shorter than predicted by simulations—possibly due to active outflows enhancing chemical segregation.

With only a handful of such studies, the mechanisms and timescales governing metal exchange between gas phases remain poorly constrained. Addressing this requires a statistically significant sample of galaxies with spatially matched UV and optical spectroscopy. To this end, we employ data from the COS Legacy Archive Spectroscopic Survey (CLASSY; D. A. Berg et al. 2022; B. L. James et al. 2022), which provides high-resolution UV spectra from the Hubble Space Telescope (HST) Cosmic Origins Spectrograph (COS) and cospatial optical spectra from ground-based facilities. CLASSY targets were selected to mirror the properties of galaxies at $z > 7$ (e.g., C. C. Steidel et al. 2014; O. Le Fèvre et al. 2015; A. E. Shapley et al. 2015; R. J. McLure et al. 2018; H. Atek et al. 2024; C. Simmonds et al. 2024), spanning stellar masses $\log(M_\star/M_\odot) \sim 6$–10, gas-phase metallicities $Z/Z_\odot \sim 0.03-1.2$, SFRs $\log(\mathrm{SFR}/M_\odot\ \mathrm{yr}^{-1}) \sim -3$–2, ionization levels $\mathrm{O}_{32} \sim -0.3-1.4$, and electron densities $10 < n_e < 1120\ \mathrm{cm}^{-3}$. This spectroscopic atlas uniquely enables systematic studies of metal mixing over a broad parameter space that parallels high-z systems ($z > 7$), extending beyond individual clusters to integrated galaxy scales.

The paper is designed as follows: we provide an overview on the observations in Section 2 and details on absorption-line fitting in Section 3. We present the neutral-gas abundances and ionization correction factors (ICFs) in Section 4 and ionized-gas abundances in Section 5. We discuss the comparison of multiphase metals in Section 7 and investigate properties affecting their distribution. We conclude our findings in Section 8.

2. Sample and Observations

2.1. CLASSY

CLASSY is an HST treasury program with COS, dedicated to creating the first high-resolution far-UV (FUV) spectral catalog of star-forming galaxies at $z \sim 0$. The targets have redshifts between $z = 0.002$ and 0.182, whose UV sources have Galaxy Evolution Explorer (GALEX) FUV magnitudes between $m_{\mathrm{FUV}} = 15.3$–19.2, ranging from $0\farcs11$ to $1\farcs6$ in diameter (as measured from the COS near-UV, NUV, acquisition images) and are primarily powered by star formation (as indicated by UV and optical emission-line diagnostics; M. Mingozzi et al. 2024, hereafter Paper VIII). A complete description of CLASSY and its scientific goals can be found in D. A. Berg et al. (2022, hereafter Paper I), including full details of the targets within the sample. While many properties are measured and presented here for the first time, we also draw on results from previous CLASSY publications, including: Lyα column densities from W. Hu et al. (2023, hereafter Paper VII); outflow velocities from X. Xu et al. (2022, hereafter Paper III); and ionized-gas abundances from K. Z. Arellano-Córdova et al. (2022, hereafter Paper V) and K. Z. Arellano-Córdova et al. (2025, hereafter Paper XII). In particular, we utilize several line properties from K. S. Parker et al. (2024, hereafter Paper XI), who performed an in-depth analysis of the neutral gas properties (column density, covering fraction, and outflow velocity) of a selection of low-ionization state (LIS) interstellar UV absorption lines (O I, Si II, S II, C II, and Al II) of the CLASSY sample.

2.2. UV Spectroscopic Data

Observation details of all of the HST/COS datasets included within CLASSY can be found in Paper I, including dataset IDs, gratings, central wavelength settings, position angles, exposure times, and rest wavelength coverage. Technical details of the methodologies involved in extracting, reducing, aligning, and coadding of the CLASSY FUV and NUV spectra can be found in B. L. James et al. (2022, hereafter Paper II). To summarize briefly here, CLASSY HLSP spectra consist of coadded G130M+G160M+G185M COS spectra covering 815–3200 Å. All CLASSY datasets were processed in a self-consistent way, in that they were all reduced via version 3.3.11 of the CalCOS pipeline. With regards to the homogeneity of the data reduction procedures employed, CLASSY contains data observed at different Lifetime Positions (LPs) on the COS FUV detector (as detailed in Table 2 of Paper I). All measurements reported in this paper were performed on the CLASSY HLSP coadded spectra provided on the CLASSY-MAST portal: https://archive.stsci.edu/hlsp/classy.

2.3. Optical Spectroscopic Data

Optical spectra for each of the CLASSY targets comprise primarily from Apache Point Observatory (APO) Sloan Digital Sky Survey (SDSS) observations, with additional observations from Large Binocular Telescope (LBT)/MODS, Very Large Telescope /MUSE/VIMOS, KECK/KCWI, and MMT telescopes/instruments. Full details concerning the optical observations and their treatment are reported in Paper I, M. Mingozzi et al. (2022, hereafter Paper IV), and Paper V. Paper V compares the SDSS, LBT, and MUSE integrated spectra for the galaxies with multiple observations, demonstrating that flux calibration issues or aperture differences do not introduce significant discrepancies in the optical ISM properties in terms of gas attenuation, density, temperature, metallicity, and SFRs.

A full suite of optical emission lines between 3700 and 9100 Å were detected for each galaxy and fit using single or multicomponent Gaussian profiles. Full details of the fitting methodology and optical line fluxes can be found in Paper IV and Paper V. Here, for consistency within the sample, we utilize optical properties derived from single, narrow component fits only. This component is also mostly associated with the bulk of ionized gas and provides the most relevant comparison with the ISM gas traced with the absorption-line profiles discussed in Section 3.

3. Absorption Line Fitting

Absorption features in the CLASSY data were fitted following the methodology applied in B. L. James et al. (2014), V. Abril-Melgarejo et al. (2024), and Paper XI, utilizing the theoretical oscillator strengths listed in Table 1. In this process, theoretical Voigt profiles were used to model the absorption lines using the Python package `VoigtFit` (J.-K. Krogager 2018), which models absorption-line profiles while taking into account the line-spread function (LSF) of the observations by convolving the intrinsic absorption profile with the instrumental LSF. This package allows absorption-line fits for each species to be optimized by simultaneously modeling different velocity components of both the target and any contaminating species from the target itself or other systems along the line of sight (e.g., the Milky Way). For each galaxy, we fitted the CLASSY coadded spectra using the appropriate LSF according to the LP of the G130M spectrum (listed in Paper I). While G160M and G185M spectral resolutions may be different, none of the ISM lines of interest to this study lie within those gratings.

This study focuses on the comparison between neutral and ionized-gas abundances. As such, only the elements who have species visible in both the UV and optical were included in our absorption profile fitting: nitrogen, sulfur, iron, and oxygen. In the UV, these species would be N I, S II, Fe II, Fe III , and O I. We also analyze P II, as it can be used to predict the O I column density (B. James & A. Aloisi 2018), and Si II and Ni II for dust depletion (Section 4.2). The optical emission-line counterparts for these species would be [N II], [S II] [S III], [Fe III], [O II], and [O III]. We also discard any galaxies for which the Lyα absorption profile was either not detected or unconstrained by Paper VII, resulting in a final sample of 31 galaxies.

Before fitting each line, continuum normalization was performed using the continuum fits detailed in Paper VII and provided as an HLSP on the CLASSY-MAST portal. Owing to the low-redshift nature of our objects ($z < 0.2$), MW ISM lines often contaminate the intrinsic ISM absorption of our individual objects. As such, a careful inspection of each target's species was made to identify all of the MW absorption features before fitting. A model was then created for each species within the target, detailing the velocity structure of the ISM (mostly single-velocity components) and of any intervening MW ISM species. With this approach, we performed a simultaneous fit to all of the lines of a species and, therefore, were able to solve for partial covering by using multiple lines with different values of $f\lambda$, where f is the oscillator strength, and λ is the rest-frame wavelength of the absorption.

In the case of P II, there is only one absorption line detected. Thus, in order to rule out partial covering, we compared the column density from the P II fit to a strong line (i.e., high f) that is not saturated, such as Fe II λ1144. Since the product of f and column density, $N(X)$, is directly proportional to the optical depth, and because the column density of P II is ~95 times weaker than that of Fe II ($\langle N(\text{P II})/N(\text{Fe II})\rangle \sim 0.05$) despite $f_{\text{PII}}/f_{\text{FeII}} = 1.5$, we are safe to assume P II is not saturated.

To enable an optimized fit, the velocity components (V_{min}) and b-parameters (i.e., the broadening of a line due to thermal and/or turbulent motion) of different species were not constrained to one another. The best-fit model profiles are estimated using a χ^2 minimization approach, with output parameters including the line column density N(X), b-parameter, redshift, and their uncertainties. An example result from this line-fitting procedure is shown in Figure 1, which shows the best-fit model for J1225+6109.

While there are numerous unresolved absorbing components along the line of sight within the COS aperture, the single-

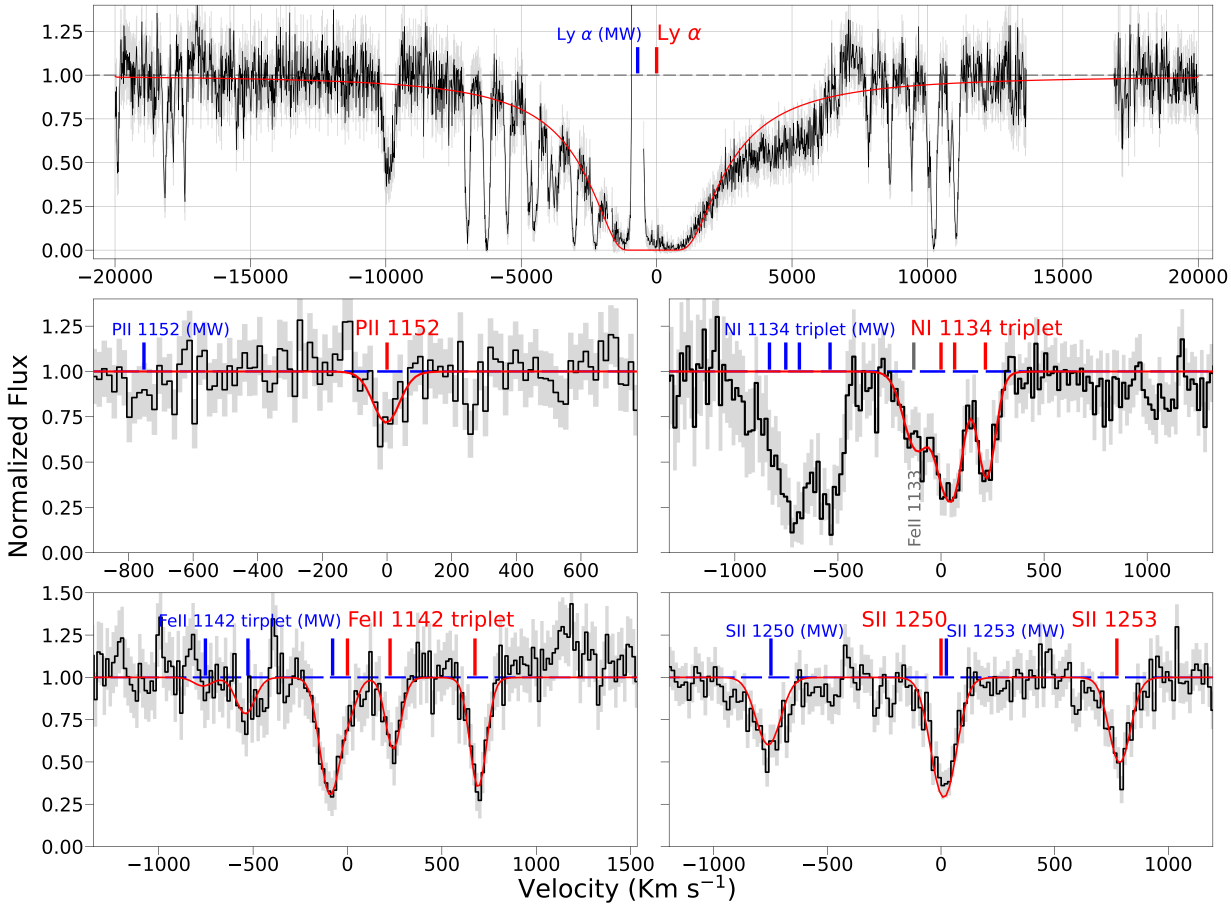

Figure 1. An example of the Voigt-fitting procedure employed within this study for J1225+6109. The top panel shows the CLASSY coadded spectrum up to ~1420 Å (in black, with errors in gray). The bottom panels show the fits for P II λ1152, the N I λ1134 triplet (1134.1, 1134.4, 1134.9 Å), Fe II λ1133, the Fe II λ1142 triplet (1142, 1143, and 1144 Å), and S II λ1250, where the galaxy and MW components in each line complex are identified with red and blue vertical markers, respectively. Each panel is centered in velocity space on the lowest wavelength line being fitted for the target within that model.

(The complete figure set (31 images) is available in the online article.)

Table 1
List of ISM Lines Fitted within This Study and Their Corresponding Oretical Parameters

Line ID	$\lambda_{\rm lab}$[a] (Å)	f[b]	Reference	Line ID	$\lambda_{\rm lab}$[a] (Å)	f[b]	Reference
Lyα	1215.6701	4.1640e-01	1	S II 1253	1253.8110	1.0880e-02	1
N I 1134.1	1134.1653	1.3420e-02	1	S II 1259	1259.5190	1.6240e-02	1
N I 1134.4	1134.4149	2.6830e-02	1	P II 1152	1152.8180	2.3610e-01	1
N I 1134.9	1134.9803	4.0230e-02	1	Fe II 1121	1121.9748	2.0200e-02	10
N I 1199	1199.5496	1.3280e-01	1	Fe II 1125	1125.4477	1.6000e-02	10
N I 1200.2	1200.2233	8.8490e-02	1	Fe II 1127	1127.0984	2.8000e-03	10
N I 1200.7	1200.7098	4.4230e-02	1	Fe II 1133	1133.6650	5.5000e-03	10
O I 1302	1302.1685	4.8870e-02	1	Fe II 1142	1142.3656	4.2000e-03	10
O I 1355	1355.5977	1.2480e-06	1	Fe II 1143	1143.2260	1.7700e-02	10
Si II 1190	1190.4158	2.9300e-01	2	Fe II 1144	1144.9379	1.0600e-01	10
Si II 1193	1193.2897	5.8400e-01	2	Fe II 1260	1260.5330	2.5000e-02	1
Si II 1260	1260.4221	1.1800e-00	2	Fe III 1122	1122.5260	7.8840e-02	1
Si II 1304	1304.3702	8.6000e-02	6	Fe III 1207	1207.0500	4.4230e-06	1
P II 1301	1301.8740	1.2710e-02	8	Fe III 1214	1214.5660	4.2730e-04	1
S II 1250	1250.5840	5.4530e-03	1	…	…	…	…

References. (1) = D. C. Morton (1991), (2) = D. A. Verner et al. (1994), (3) = W. L. Wiese et al. (1996), (4) = D. C. Morton (2003), (5) = S. Majumder et al. (2002), (6) = L. Spitzer & L. Fitzpatrick (1993), (7) = D. A. Verner et al. (1996), (8) = A. Hibbert (1988), (9) = S. S. Tayal (1995), (10) = J. C. Howk et al. (2000), (11) = J. Zsargo & S. R. Federman (1998).

[a] Vacuum wavelengths from D. C. Morton (1991).

[b] Oscillator strengths from references indicated in column (4).

velocity component fitting is appropriate here, as the derived kinematical properties represent an effective average over a distribution of unresolved structures (see I. Clark et al. 2024). As originally demonstrated by E. B. Jenkins (1986), ensembles of unresolved absorbing components can be reliably analyzed using a single-component approximation, even in the presence of variations in *b*-parameters and saturation, provided that the transitions are not strongly saturated. More recent work has reinforced and clarified this conclusion. In particular, J. X. Prochaska (2006) demonstrated that unresolved saturation primarily biases column densities derived from heavily saturated transitions, while reliable measurements can be recovered when multiple lines spanning a range of oscillator strengths are used to constrain the fits. In this regime, the single-component *b*-parameter should be interpreted as an effective velocity dispersion that encapsulates thermal broadening, turbulence, and unresolved kinematic substructure, whereas the column density is anchored by the weakest available transitions. Accordingly, our abundance analysis is restricted to elements and transitions for which unsaturated are available—most notably N, S, and Fe—while species dominated by strong absorption (e.g., O I, C II) are excluded or inferred indirectly. This framework underpins our fitting strategy and motivates our exclusion of saturated lines from the abundance analysis.

One of the most challenging issues in absorption-line fitting is saturation. Saturation can manifest in three ways: classical saturation, hidden saturation, or partial covering. While classical saturation is relatively straightforward to identify, since the equivalent width increases while the line core becomes optically thick (essentially 'bottoming-out' the line), hidden saturation and partial covering are more subtle. In the former case, multiple unresolved velocity components along the line of sight can produce an apparently unsaturated profile; in the latter, the absorbing gas does not fully cover the background continuum source, leading to residual flux in the line core and an underestimated column density.

W. Hu et al. (2023) reported evidence for partial covering in several Lyα damping profiles, where the extremely large optical depth of Lyα makes even small deviations from unity covering fraction readily detectable. The residual flux in these cases likely reflects the spatially extended stellar continuum within the COS aperture that is not fully covered by patchy neutral gas. In contrast, the low-ionization metal lines used here are constrained through simultaneous fits to multiple transitions spanning a range of oscillator strengths. If significant partial covering were present, transitions with different $f\lambda$ values would yield inconsistent column densities. Instead, when a single model (column density, *b*-parameter, and velocity centroid) reproduces all available transitions, the solutions are anchored by the weakest lines and are therefore robust against moderate saturation or small covering-fraction deviations. Within the S/N of the CLASSY spectra, the metal lines used for abundance measurements reach zero flux in their cores within uncertainties, and any departure from unity covering fraction must therefore be small enough not to measurably bias the derived column densities.

Lines affected by classical saturation in this study are those with large oscillator strengths (e.g., O I λ1302 with $f = 4.8870 \times 10^{-2}$, hence the need to predict N(O I) using P II and S II, as discussed below). Hidden saturation is most easily identified by fitting lines with different $f\lambda$ values of the same species. As such, careful tests were performed for each ion with multiple transitions by separately fitting the weakest line and comparing the output with that obtained when fitting all lines simultaneously. In cases where the fit to the weakest line overpredicted the strength of the stronger transitions, we adopted the column density derived from the weakest line alone. If multiple lines of the same ion could be reproduced by a single model, they were deemed free of significant hidden saturation or partial covering. A detailed discussion of these effects can be found in B. L. James et al. (2014), including an example for the Fe II λ1142,λ1143,λ1144 triplet.

In cases where species were isolated (i.e., uncontaminated by either other species from the target itself or the MW), we utilized column-density measurements from Paper XI, which only measured isolated or uncontaminated ISM profiles. In doing so, the methodology adopted by Paper XI differed slightly from that utilized here in that the *b*-parameter and velocity was held fixed between different species. When performing our line fits, we adopted the same *b*-parameter as Paper XI as an initial value and allowed it to vary. If this *b*-parameter provided a satisfactory fit to that particular line, as assessed via the χ^2 value of the fit and a visual inspection of the model and residual fit, we adopted it as a fixed value. This was particularly helpful when fitting weak transitions, like P II λ1152 (D. C. Morton 1991).

To check for consistency between the two methodologies, comparisons were made between the S II λ1253,1259 profile fits reported by Paper XI and those measured here for the same systems. In the majority of cases, differences of 0.5–1 dex were found for N(S II), which we attribute to the different *b*-parameters applied for many of the fits and, as noted in Paper XI, their N(S II) values were often inflated because they were not taking into account the contamination of S II λ1259 by Si II λ1260.

For the purpose of this study, we only adopt the Paper XI column densities derived from O I λ1302 line, which, due to saturation issues, we use only to calculate a lower limit on O/H for a comparison with the O/H value derived from other species (discussed in Section 4). We only use the O I λ1302 from Paper XI because this is the only line that overlaps between the two studies that is truly isolated.

Finally, we note that the COS aperture integrates the continuum from multiple bright knots and their associated neutral/photodissociation region (PDR) gas, so the observed absorption profiles represent a continuum-flux-weighted average over unresolved sight lines. In the weak-line regime relevant to our abundance work, this averaging behaves approximately linearly and yields the flux-weighted mean optical depth (E. B. Jenkins 1986; J. X. Prochaska 2006). In contrast, mixing saturated components is nonlinear and can bias columns low; we mitigate this by (i) prioritizing weak transitions, (ii) enforcing multiline fits across a range of oscillator strengths to test for hidden saturation and partial covering, and (iii) fitting covering fractions when indicated (Section 3; see also B. L. James et al. 2014). With the present data, we cannot robustly measure sight-line-to-sight-line column-density variations within each UV aperture, so we interpret our derived columns as continuum-flux-weighted means. Under plausible spatial variations on resolved scales ($\lesssim$0.5 dex between bright knots; S. Hernandez et al. 2021; V. Abril-Melgarejo et al. 2024), the resulting bias in weak-line columns is $\lesssim$0.2 dex, which is smaller than our measurement uncertainties (0.3–0.5 dex). Empirically, the low-ionization species used for abundances (N I, O I, S II, Fe II) exhibit consistent kinematics (similar centroids and widths), indicating that they probe the same neutral/PDR structures rather than distinct regions within the aperture. Consequently, any aperture-averaging effects are expected to impact these ions similarly and, within our quoted uncertainties, remain subdominant relative to other error sources.

The best-fit parameters for each galaxy are listed in Table 8 within Appendix A, including column density, and *b*-parameter. Lines affected by saturation are listed with lower-limit column densities and are excluded from the analysis presented in Section 6. We also include the H I column densities from Paper VII for completeness. We refer the reader to Paper VII for a full description of the Lyα fitting procedure, uncertainty analysis, and a complete set of figures illustrating the Lyα fits. The uncertainties on N(H I) were derived using a Markov Chain Monte Carlo approach in which the spectra were perturbed according to the flux errors and refit 1000 times, with the 16th and 84th percentiles adopted as the confidence interval. For the highest-S/N systems (in particular J0337−0502 and J0934+5514), the formal statistical uncertainty on $\log N$(H I) is 0.004 and 0.002 dex, respectively, reflecting the high S/N and spectral resolution of the data.

4. Neutral-gas Abundances

Chemical abundances for the neutral gas were derived from the UV absorption lines of the LISs listed in Table 2 and were derived via the ratio of the ion column density with the H I column density, i.e., $\log(X/\mathrm{H}) = \log(N(X)) - \log(N(\mathrm{HI}))$. For calculating abundances relative to solar, we obtain solar abundance values from M. Asplund et al. (2021). These are listed in Table 3, alongside the abundances corrected for ionization levels along the line of sight, which we describe below in Section 4.1.

Obtaining a true “apples-to-apples” comparison of ionized-gas and neutral-gas abundances is of paramount importance for this study. Oxygen is traditionally used as a benchmark for the ionized-gas metallicity of a galaxy, as it is one of the strongest emitting species in the optical. Unfortunately, oxygen can be very challenging to constrain in the neutral ISM for two reasons: (i) the O I λ1302 line suffers from classical saturation due to its strength (and O I λ1355 is undetected); (ii) in low-redshift objects, O I λ1302 is often contaminated by Geocoronal emission at ∼1304 Å.

To circumvent the challenges associated with oxygen, we derive oxygen abundances following the methodology of B. James & A. Aloisi (2018) via the column densities of S II and P II. To describe briefly, B. James & A. Aloisi (2018) used relationships between the O I, S II, and P II column densities as robust proxies to estimate O/H abundances in the neutral gas of different environments (with regards to metallicity, SFR, and N(H I)).

In Table 4, we list both the lower-limit oxygen abundances derived from O I λ1302, which were inferred from Paper XI, and oxygen abundances inferred from N(S II) and N(P II) proxies (log(O(P,S)/H)). The latter represents the average of log(O(P)) and log(O(S)). In the cases where N(S II) or N(P II) were not available, only one proxy relationship was used. On average, log(O(P, S)/H) is greater than the lower limit on log (O/H) derived from O I λ1302 by ∼0.86 dex.

Table 2
Classification of Neutral versus Ionized Spectroscopic Features Measured within This Study, where the Delineation between the Two Phases Is Made According to the Dominant Ionization Stage of Hydrogen

Element	Neutral	Ionized
H	H I	H II (13.6)
N	N I	[N II] (14.5)
O	O I	[O II] (13.6), [O III] (35.1)
Si	Si II (8.15)	Si III (16.3), Si IV (33.5)
P	P II (10.5)	
S	S II (10.36)	[S II] (10.36), [S III] (23.3)
Fe	Fe II (7.90)	[Fe II] (7.90), [Fe III] (16.2)

Note. The forbidden metal lines listed here are measured from optical emission lines, whereas permitted metal lines are those measured from UV absorption lines. Numbers in parentheses refer to the ionization potential energy required to create that feature.

4.1. Ionization Correction Factors

In order to accurately determine the abundance of metals in the neutral ISM gas, the ionization state of the gas along the line of sight needs to be accounted for using ICFs, which depend on the gas structure of the system.[12] Note that neutral-gas ICFs are different from the ICFs used in ionized-gas chemical abundance calculations, which instead account for missing ionic species in the ionized gas due to observational constraints (wavelength, resolution, depth, etc). As such, we refer them as “neutral-gas ICFs” hereafter to avoid confusion between the two concepts.

Neutral-gas ICFs were derived for each system following the methodology first described in B. L. James et al. (2014) and incorporated by S. Hernandez et al. (2020) and V. Abril-Melgarejo et al. (2024). In Appendix A we provide a full overview of the modeling concepts involved, which are designed to ensure that we correctly account for the total amount of the element within the neutral gas. A schematic representation of the ICF modeling structure is shown in Figure 2, where we illustrate how the two components of the neutral-gas ICFs (the neutral ICF, ICF$_{\mathrm{neu.}}$, and the ionized ICF, ICF$_{\mathrm{ion.}}$) are calculated according to a line-of-sight geometry. The dominant spectroscopic feature within the “neutral” (N(H I)>N(H II)) and “ionized” (N(H II)>N(H I)) zones of the ISM can be found in Table 2.

Overall, the size of ICF$_{\mathrm{neu.}}$ and ICF$_{\mathrm{ion.}}$ are comparable for most species and essentially cancel each other out to result in a very small ICF$_{\mathrm{tot.}}$ (see Equation (A4) in Appendix A). The exceptions are nitrogen and oxygen, where ICF$_{\mathrm{neu.}}$ is larger than ICF$_{\mathrm{ion.}}$ by up to ∼0.3 dex for the systems with highest metallicity, lowest N(H I), and highest UV luminosity (see Figure 16). This is because N I and O I have comparable ionization potentials (IP = 14.53 eV and 13.62 eV, respectively) that are only slightly larger than hydrogen’s (IP = 13.58 eV) (see Table 2). Thus, N and O are in their neutral form within the neutral ISM (compared to S II, Fe II, and P II, which are singly ionized). As such, we need to account for nonnegligible amounts of N II and O II that lie outside the PDR, and very small amounts of N I and O I that lie within the PDR (essentially defined according to the IP of

---

[12] Although UV absorption probes cool gas along the full line of sight and may include some CGM contribution, the narrow, symmetric profiles centered near systemic velocity indicate that the measured column densities are dominated by the neutral ISM.

Table 3
Neutral Gas Abundances Before and After Applying ICFs Listed in Table 9

Target	$\log(\mathrm{N/H})$	$\log(\mathrm{N/H})_{ICF}$	$\log(\mathrm{O}_{(P,S)}/\mathrm{H})$	$\log(\mathrm{O/H})_{ICF}$	$\log(\mathrm{S/H})$	$\log(\mathrm{S/H})_{ICF}$	$\log(\mathrm{Fe/H})$	$\log(\mathrm{Fe/H})_{ICF}$
J0127-0619	6.29 ± 0.29	6.29 ± 0.29	8.02 ± 0.4	8.04 ± 0.4	6.56 ± 0.27	6.57 ± 0.27	5.98 ± 0.29	5.98 ± 0.29
J0144+0453	6.17 ± 0.09	6.03 ± 0.09	8.61 ± 0.21	8.77 ± 0.21	7.04 ± 0.08	7.09 ± 0.08	6.86 ± 0.22	6.77 ± 0.22
J0337-0502	5.02 ± 0.02	5.02 ± 0.02	6.6 ± 0.15	6.61 ± 0.15	5.15 ± 0.03	5.16 ± 0.03	5.51 ± 0.04	5.51 ± 0.04
J0405-3648	5.65 ± 0.38	5.64 ± 0.38	7.74 ± 0.16	7.8 ± 0.16	6.1 ± 0.11	6.13 ± 0.11	6.09 ± 0.33	6.09 ± 0.33
J0823+2806	6.19 ± 0.23	6.19 ± 0.23	7.99 ± 0.04	8 ± 0.04	6.42 ± 0.04	6.43 ± 0.04	6.19 ± 0.34	6.19 ± 0.34
J0934+5514	5.3 ± 0.06	5.29 ± 0.06	7.29 ± 0.2	7.33 ± 0.2	5.72 ± 0.05	5.74 ± 0.05	5.57 ± 0.06	5.57 ± 0.06
J0938+5428	6.48 ± 0.09	6.26 ± 0.09	8.67 ± 0.16	8.78 ± 0.16	6.92 ± 0.11	6.88 ± 0.11	6.39 ± 0.14	6.24 ± 0.14
J0940+2935	5.46 ± 0.05	5.46 ± 0.05	7.66 ± 0.4	7.67 ± 0.4	6.12 ± 0.38	6.13 ± 0.38	6.16 ± 0.41	6.17 ± 0.41
J0944+3442	5.6 ± 0.06	5.6 ± 0.06	7.69 ± 0.13	7.71 ± 0.13	…	…	5.22 ± 0.21	5.22 ± 0.21
J0944-0038	5.62 ± 0.07	5.62 ± 0.07	7.9 ± 0.23	7.91 ± 0.23	5.78 ± 0.21	5.79 ± 0.21	6.14 ± 0.38	6.14 ± 0.38
J1024+0524	5.74 ± 0.1	5.65 ± 0.1	8.21 ± 0.21	8.32 ± 0.21	6.58 ± 0.09	6.59 ± 0.09	6.2 ± 0.21	6.13 ± 0.21
J1025+3622	5.65 ± 0.23	5.61 ± 0.23	8.14 ± 0.21	8.18 ± 0.21	6.57 ± 0.21	6.61 ± 0.21	6.86 ± 0.23	6.85 ± 0.23
J1044+0353	5.63 ± 0.32	5.63 ± 0.32	7.25 ± 0.1	7.25 ± 0.1	5.63 ± 0.05	5.63 ± 0.05	5.74 ± 0.09	5.74 ± 0.09
J1105+4444	5.52 ± 0.08	5.52 ± 0.08	7.57 ± 0.12	7.58 ± 0.12	6.06 ± 0.08	6.06 ± 0.08	5.86 ± 0.13	5.86 ± 0.13
J1119+5130	5.45 ± 0.1	5.43 ± 0.1	7.94 ± 0.19	8.01 ± 0.19	6.42 ± 0.12	6.45 ± 0.12	6.87 ± 0.5	6.87 ± 0.5
J1129+2034	6.37 ± 0.09	6.37 ± 0.09	8.11 ± 0.12	8.14 ± 0.12	6.63 ± 0.09	6.65 ± 0.09	6.16 ± 0.1	6.16 ± 0.1
J1132+1411	6.64 ± 0.03	6.59 ± 0.03	8.83 ± 0.15	8.91 ± 0.15	7.45 ± 0.09	7.5 ± 0.09	6.75 ± 0.07	6.73 ± 0.07
J1132+5722	5.54 ± 0.05	5.54 ± 0.05	7.48 ± 0.23	7.5 ± 0.23	6.04 ± 0.09	6.05 ± 0.09	5.68 ± 0.09	5.68 ± 0.09
J1144+4012	6.56 ± 0.11	6.49 ± 0.11	8.6 ± 0.09	8.62 ± 0.09	7.03 ± 0.09	7.05 ± 0.09	7.12 ± 0.35	7.09 ± 0.35
J1148+2546	5.68 ± 0.05	5.68 ± 0.05	7.92 ± 0.11	7.97 ± 0.11	6.26 ± 0.05	6.28 ± 0.05	6.43 ± 0.08	6.43 ± 0.08
J1150+1501	6.41 ± 0.26	6.41 ± 0.26	7.98 ± 0.15	8.02 ± 0.15	6.48 ± 0.04	6.5 ± 0.04	5.86 ± 0.12	5.87 ± 0.12
J1225+6109	6.06 ± 0.14	6.06 ± 0.14	7.7 ± 0.15	7.73 ± 0.15	6.17 ± 0.05	6.19 ± 0.05	5.92 ± 0.12	5.92 ± 0.12
J1253-0312	6.37 ± 0.12	6.37 ± 0.12	7.55 ± 0.07	7.59 ± 0.07	…	…	6.19 ± 0.19	6.19 ± 0.19
J1314+3452	6.46 ± 0.37	6.45 ± 0.37	8.3 ± 0.08	8.37 ± 0.08	6.74 ± 0.06	6.78 ± 0.06	6.07 ± 0.06	6.08 ± 0.06
J1359+5726	…	…	7.34 ± 0.26	7.36 ± 0.26	5.78 ± 0.17	5.79 ± 0.17	5.45 ± 0.27	5.45 ± 0.27
J1416+1223	7.28 ± 0.34	6.92 ± 0.34	8.52 ± 0.8	8.49 ± 0.8	7.1 ± 0.1	6.97 ± 0.1	7.11 ± 0.2	6.88 ± 0.2
J1418+2102	5.55 ± 0.05	5.55 ± 0.05	7.45 ± 0.12	7.47 ± 0.12	5.97 ± 0.06	5.99 ± 0.06	5.85 ± 0.18	5.85 ± 0.18
J1444+4237	5.32 ± 0.06	5.32 ± 0.06	7.44 ± 0.27	7.44 ± 0.27	6.06 ± 0.18	6.06 ± 0.18	5.94 ± 0.72	5.94 ± 0.72
J1448-0110	5.84 ± 0.35	5.84 ± 0.35	7.53 ± 0.17	7.54 ± 0.17	6.01 ± 0.04	6.02 ± 0.04	5.88 ± 0.08	5.88 ± 0.08
J1521+0759	6.06 ± 0.81	5.82 ± 0.81	8.43 ± 0.17	8.56 ± 0.17	…	…	6.05 ± 0.12	5.88 ± 0.12
J1545+0858	5.15 ± 0.06	5.15 ± 0.06	7.28 ± 0.4	7.31 ± 0.4	…	…	5.43 ± 0.11	5.44 ± 0.11

hydrogen), as illustrated in Figure 2. This results in an overall positive $\mathrm{ICF}_{\mathrm{tot.}}$ and net increase to account for the full amount of N and O within the "neutral" zone. Fe (IP = 7.90 eV) and Ni (IP = 7.64 eV) have similarly high ICFs, with ICF_{tot} reaching up to ∼0.2 dex in the same "extreme" systems described above.

The total ICFs ($\mathrm{ICF}_{\mathrm{total}}$) computed for each galaxy are presented in Table 9 and used to compute the ICF-corrected abundances ($\log(\mathrm{X/H})_{\mathrm{ICF}}$) listed in Table 3.

4.2. Dust Depletion

The depletion Δ_{X} of an element X is defined as the amount of element X incorporated into the dust grains. Understanding dust depletion is essential to decipher both the origin of dust (see, e.g., L. Mattsson et al. 2019; C. Konstantopoulou et al. 2022) and to estimate the total abundance of different elements within the gas (see, e.g., A. De Cia et al. 2016, 2018; C. Konstantopoulou et al. 2024). A. De Cia et al. (2016) studied the dust depletion in the local Universe (Milky Way) and high-redshift gas clouds (using damped Lyα systems, or DLAs) and came up with a formalism that calculates the depletion of different metals onto dust independent of their gas-phase metallicity. However, studies have shown that the overall depletion strength increases with metallicity, as more metals become available to condense onto dust grains (e.g., E. B. Jenkins 2009; P. Wiseman et al. 2017; A. De Cia et al. 2018). At low metallicities, the reduced dust-to-gas ratio and slower grain growth lead to weaker depletions, particularly for volatile elements, while refractory elements (such as Fe, Ni, and Si) remain more strongly affected even in metal-poor environments.

We use the most updated version of the A. De Cia et al. (2024) formalism (see their Equations (1)–(5)) to estimate the dust depletion and calculate the depletion-corrected abundance of different metals observed within our sample of CLASSY galaxies. Calculations are made using all available refractory elements within the CLASSY spectra using the column densities of Fe II, Ni II, and Si II, relative to H I. The constants ($A2_x$ and $B2_x$) required for each metal to implement this depletion-correction formalism were taken from C. Konstantopoulou et al. (2022, 2024).

Figure 3 shows the correction for depletion, $\Delta\log(\mathrm{X/H})_{\mathrm{dep}}$, required for different metals (X = Fe, S, and O) for each galaxy in our sample. Nitrogen is not included here because it is not a refractory element and so does not deplete onto dust. For 28/31 of the galaxies within our sample, we only have lower limits for depletion (since the $v \sim 0\,\mathrm{km\,s^{-1}}$ ISM component of silicon is saturated for these systems).

For the three galaxies with unsaturated silicon and available hydrogen column densities, the average depletion correction for elements Fe, S, and O are ∼0.7, 0.2 and 0.05, respectively. These average depletion levels are in agreement with previous studies, where Fe is known to deplete heavily onto dust grains, whereas S and O are far less depleted (e.g., E. B. Jenkins 2009; B. James & A. Aloisi 2018); although typically, O should be slightly more depleted than S (A. De Cia et al. 2016). However, given the small sample size and large uncertainties

Table 4
Neutral Gas Oxygen Abundances Derived from Phosphorus (O(P)/H) and Sulfur (O(S)/H), and the Average from both P and S (O(P,S)/H), as Described in Section 4

Target	log(O(P)/H)	log(O(S)/H)	log(O(P,S)/H)	log(O/H)
J0127-0619	7.65 ± 0.29	7.91 ± 0.27	7.80 ± 0.40	< 7.46
J0144+0453	8.62 ± 0.20	8.61 ± 0.08	8.61 ± 0.21	< 7.50
J0337-0502	6.44 ± 0.15	6.72 ± 0.03	6.60 ± 0.15	< 7.32
J0405-3648	7.81 ± 0.11	7.67 ± 0.11	7.74 ± 0.16	…
J0823+2806	…	7.99 ± 0.04	7.99 ± 0.04	< 6.61
J0934+5514	7.29 ± 0.19	7.29 ± 0.05	7.29 ± 0.20	< 7.80
J0938+5428	8.79 ± 0.12	8.49 ± 0.11	8.67 ± 0.16	< 7.87
J0940+2935	7.62 ± 0.12	7.69 ± 0.38	7.66 ± 0.40	< 6.16
J0944+3442	7.69 ± 0.13	…	7.69 ± 0.13	< 6.10
J0944-0038	8.13 ± 0.10	7.35 ± 0.21	7.90 ± 0.23	< 6.77
J1024+0524	< 8.27	8.15 ± 0.09	8.15 ± 0.09	< 6.95
J1025+3622	…	8.14 ± 0.21	8.14 ± 0.21	< 7.83
J1044+0353	7.28 ± 0.45	7.19 ± 0.44	7.24 ± 0.63	< 7.89
J1105+4444	7.47 ± 0.12	7.59 ± 0.12	7.53 ± 0.17	< 5.72
J1119+5130	7.89 ± 0.15	7.99 ± 0.12	7.94 ± 0.19	< 7.04
J1129+2034	7.99 ± 0.09	8.20 ± 0.09	8.11 ± 0.12	< 6.68
J1132+1411	8.49 ± 0.11	9.02 ± 0.09	8.83 ± 0.15	< 7.38
J1132+5722	7.29 ± 0.21	7.61 ± 0.09	7.48 ± 0.23	< 6.62
J1144+4012	…	8.60 ± 0.09	8.60 ± 0.09	< 7.66
J1148+2546	8.00 ± 0.10	7.83 ± 0.05	7.92 ± 0.11	< 7.17
J1150+1501	7.91 ± 0.14	8.05 ± 0.04	7.98 ± 0.15	< 7.06
J1225+6109	7.66 ± 0.14	7.74 ± 0.05	7.70 ± 0.15	…
J1253-0312	7.55 ± 0.07	…	7.55 ± 0.07	< 5.97
J1314+3452	8.29 ± 0.05	8.27 ± 0.04	8.28 ± 0.07	< 6.93
J1359+5726	7.30 ± 0.23	7.39 ± 0.42	7.35 ± 0.48	< 6.24
J1416+1223	< 8.29	8.67 ± 0.10	8.67 ± 0.10	< 7.78
J1418+2102	7.32 ± 0.10	7.54 ± 0.06	7.45 ± 0.12	< 6.49
J1444+4237	7.09 ± 0.20	7.63 ± 0.18	7.44 ± 0.27	< 7.79
J1448-0110	7.46 ± 0.17	7.58 ± 0.04	7.53 ± 0.17	< 6.57
J1521+0759	8.43 ± 0.17	…	8.43 ± 0.17	< 8.00
J1545+0858	7.28 ± 0.40	…	7.28 ± 0.40	< 7.02

Note. Oxygen abundances derived from the saturated O I λ1302 line are provided as lower limits for comparison.

associated with the average depletion corrections, we do not implement a depletion-correction in the remaining analysis.

5. Ionized-gas Abundances

Ionized-gas abundances were taken from Paper IV, Paper V, and Paper XII, which contain full details of the calculations and ionized-gas ICF corrections, and from this work for Fe/H. We include Fe in this multiphase abundance study for two reasons—first, Fe/H is well measured in the neutral gas (owing to the Fe II$\lambda\lambda$1142,43,44 triplet). Second, Fe provides important insight into the long-term chemical-evolutionary status of the CLASSY galaxies, as Fe is produced predominantly by SNe Ia on timescales longer than ∼1 Gyr (e.g., C. Kobayashi et al. 2020).

To determine the ionic abundances of Fe^{2+} in the ionized-gas phase, we used the dust-corrected fluxes of [Fe III] λ4658 for 25 CLASSY galaxies reported in Paper IV that have both neutral and ionized Fe/H abundances and followed the procedure presented in Paper XII. Multiple Fe emission lines are seen in H II regions, such as [Fe II], [Fe III], [Fe IV], and [Fe V]. However, we used [Fe III] λ4658 alone to characterize the abundance of Fe, as [Fe II] can be affected by fluorescence and [Fe IV] is inherently weak (e.g., M. Rodríguez 1999; M. Rodríguez & R. H. Rubin 2005; D. A. Berg et al. 2021; J. E. Méndez-Delgado et al. 2024). We calculated the $\mathrm{Fe}^{+2}/\mathrm{H}^{+}$ ionic abundance using `PyNeb` with the transition probabilities from P. Quinet (1996) and collision strengths from H. Zhang (1996). We adopted physical conditions derived from ions with similar ionization potentials as [Fe III] (16.2 eV), namely T_e[O II] (or T_e[N II]) and n_e[S II]).

One of the most critical aspects to derive the total abundances of Fe (and other elements) is the selection of appropriate ionized-gas ICFs (e.g., M. Rodríguez & R. H. Rubin 2005; Y. I. Izotov et al. 2006; D. A. Berg et al. 2021; J. E. Méndez-Delgado et al. 2024). In J. E. Méndez-Delgado et al. (2024), the authors analyzed the performance of the Fe ICF using a sample of star-forming regions with measurements of different ionization states of Fe (i.e., $\mathrm{Fe}^{+}/\mathrm{H}^{+}$, $\mathrm{Fe}^{2+}/\mathrm{H}^{+}$, $\mathrm{Fe}^{3+}/\mathrm{H}^{+}$, and $\mathrm{Fe}^{4+}/\mathrm{H}^{+}$). The total Fe/H abundance derived without using an ICF (i.e., a "robust" Fe/H obtained by summing all of the observed states) was then compared with the Fe/H values obtained by applying the Fe ICFs from M. Rodríguez & R. H. Rubin (2005) and Y. I. Izotov et al. (2006), which utilize the observed $\mathrm{Fe}^{2+}/\mathrm{H}^{+}$. J. E. Méndez-Delgado et al. (2024) found that Fe/H abundances derived using the ICF from M. Rodríguez & R. H. Rubin (2005) agree more closely with the "robust" Fe/H estimates than those based on the ICF of Y. I. Izotov et al. (2006), with deviations of $\lesssim$0.2 dex versus discrepancies as large as ∼0.7 dex for the latter. In this study, we used the Fe ionized-gas ICF proposed by M. Rodríguez & R. H. Rubin (2005) to take into account the contribution of Fe^{+} and Fe^{3+}. Additionally, we stress that Fe can be significantly depleted onto dust grains, making it difficult to mitigate any bias derived only from the ICF. In Table 5 we list the total CLASSY abundances of Fe/H and other elements used in this work.

6. Results

To summarize this work so far, all absorption-line abundances presented here include corrections for unobserved ionization stages. In practice, this means each species is accounted for in both the neutral and ionized zones as defined by hydrogen. Since the first ionization potentials of the neutral species S I (10.36 eV), Fe I (7.9 eV), and P I (10.49 eV) are below 13.6 eV, their singly ionized stages (S II, Fe II, and P II; see Table 2) can arise in both neutral gas and in H II regions/PDRs. Their nonneutral contribution has therefore been removed through $\mathrm{ICF}_{\mathrm{ion.}}$. Although many species are not truly neutral in the "neutral zone," we refer to the resulting quantities as neutral-gas abundances because they trace the metals associated with neutral hydrogen.

In this section, we directly compare the ICF-corrected neutral-gas abundances ($\mathrm{X}/\mathrm{H}_{\mathrm{neu}}$, Table 3) with the (also ICF-corrected) ionized-gas abundances ($\mathrm{X}/\mathrm{H}_{\mathrm{ion}}$, Table 5), first as a one-to-one comparison and then in a nucleosynthetic context by assessing the multiphase abundance ratios (N/O, S/O, α/Fe) as a function of metallicity (i.e., 12+log(O/H) for the ionized gas).

6.1. Neutral- versus Ionized-gas Abundances

In Figures 4(a)–(d), we plot the ionized and neutral-gas abundances for nitrogen, oxygen, sulfur, and iron, along with the 1:1 ratio (black dashed line). We define the offset in abundance between the two phases as $\Delta\mathrm{X}/\mathrm{H} = \mathrm{X}/\mathrm{H}_{\mathrm{neu.}} - \mathrm{X}/\mathrm{H}_{\mathrm{ion.}}$, such that a positive $\Delta(\mathrm{X}/\mathrm{H})$ implies a higher abundance of X in the neutral gas. All $\Delta\mathrm{X}/\mathrm{H}$ values are listed in Table 6.

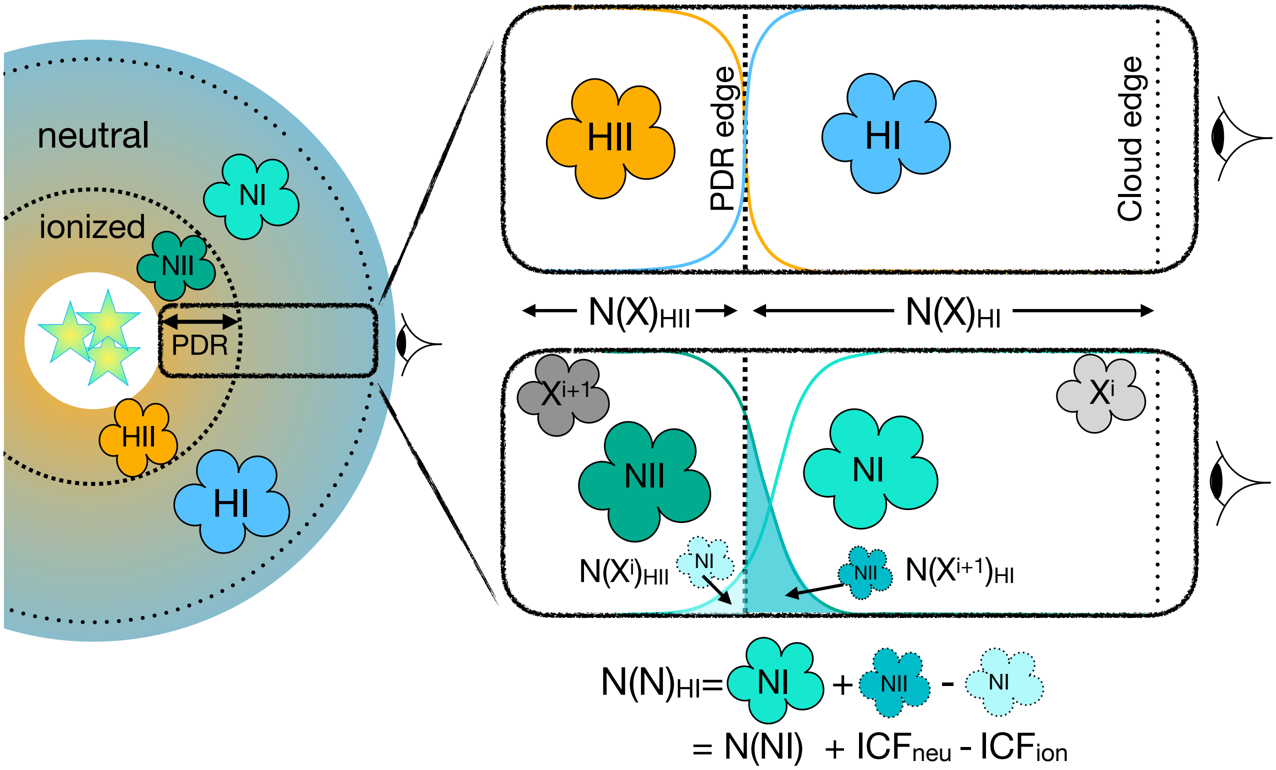

Figure 2. Schematic representation of the neutral-gas ionization correction factor (ICF) modeling structure described in Section 4.1, shown here using nitrogen as an example. The edges of the ionized and neutral gas zones are defined by hydrogen (the photodissociation region). A zoomed-in area of a gas column, which contains both the PDR and cloud edge, is shown in the right panels, depicting the ionization structure of H II and H I (top) and N II and N I (bottom).

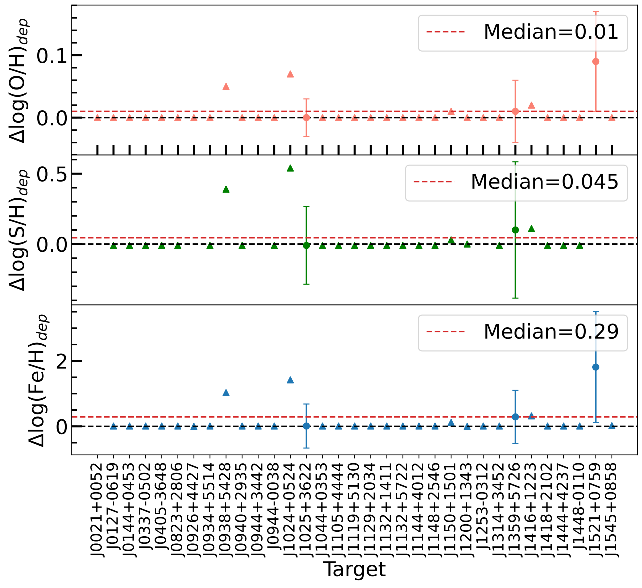

Figure 3. Depletion corrections for O, S, and Fe for each of the galaxies within our sample. The dashed black and red horizontal lines in each panel show no depletion and average depletion value for each element, respectively. Triangles represent lower limits.

6.1.1. Oxygen and Sulfur

For α-elements O and S, which are mostly produced on short timescales (5–100 Myr) via core collapse (Type II SNe; e.g., C. Kobayashi et al. 2020), there is a good agreement between the two phases. The average offset for sulfur is small, albeit with a relatively large amount of scatter ($\langle \Delta \mathrm{S/H} \rangle = 0.15 \pm 0.38$). Similarly, oxygen shows a good agreement between the phases and large amount of scatter ($\langle \Delta \mathrm{O/H} \rangle = 0.03 \pm 0.44$), which may be due to the fact that $\mathrm{O/H_{neu.}}$ is derived from a combined average of sulfur and phosphorus using the relation described above. Another contributing factor to the amount of scatter seen here is the lack of dust depletion corrections, which would typically affect O more than S in low-metallicity environments (E. B. Jenkins 2009; A. De Cia et al. 2016).

6.1.2. Iron

For iron, which is produced primarily in Type Ia SNe on ∼1 Gyr timescales (∼60% contribution) and to a lesser extent in core-collapse SNe (CCSNe) on 5–100 Myr timescales (∼40%), the CLASSY galaxies show $\mathrm{Fe/H_{neu.}} > \mathrm{Fe/H_{ion.}}$, with $\langle \Delta \mathrm{Fe/H} \rangle = 0.25 \pm 0.47$. The large dispersion indicates that, on average, Fe is broadly well mixed between the two phases. In Figure 4(d) we show both the ICF and ICF +depletion-corrected Fe/H values for the neutral gas, applying the depletion factor to the three galaxies for which it can be constrained ($\mathrm{Fe/H_{dc}}$). This correction increases $\langle \Delta \mathrm{Fe/H} \rangle$ to 0.66 ± 0.61. If we were to adopt the average Fe depletion correction of ∼0.7 dex for all galaxies (see Section 4.2), the offset between the phases would increase further to $\langle \Delta \mathrm{Fe/H} \rangle \sim 0.9$. Considering that 28/31 galaxies have only lower-limit depletion corrections, it is likely that $\mathrm{Fe/H_{neu.}}$ exceeds $\mathrm{Fe/H_{ion.}}$ in most systems.

The deficit of Fe in the ionized gas likely reflects ongoing dust depletion and grain formation in CCSNe ejecta, which efficiently lock Fe into dust while leaving α-elements such as O and S largely in the gas phase (e.g., M. Rodríguez & R. H. Rubin 2005; M. Matsuura et al. 2011; I. De Looze et al.

Table 5
Ionized-gas Abundances after Applying ICF Corrections

Target	$\log(N/H)_{\rm ion}$	$\log(O/H)_{\rm ion}$	$\log(S/H)_{\rm ion}$	$\log(Fe/H)_{\rm ion}$
J0127-0619	6.66 ± 0.14	7.52 ± 0.08	6.08 ± 0.03	…
J0144+0453	5.83 ± 0.22	7.45 ± 0.08	…	…
J0337-0502	5.91 ± 0.06	7.23 ± 0.01	5.43 ± 0.01	5.36 ± 0.07
J0405-3648	5.98 ± 0.15	7.28 ± 0.07	5.54 ± 0.03	5.36 ± 0.15
J0823+2806	7.16 ± 0.16	8.25 ± 0.10	6.55 ± 0.02	6.18 ± 0.04
J0934+5514	…	7.09 ± 0.02	…	5.29 ± 0.19
J0938+5428	7.02 ± 0.15	8.26 ± 0.08	6.59 ± 0.03	5.99 ± 0.07
J0940+2935	6.23 ± 0.20	7.98 ± 0.23	6.15 ± 0.05	…
J0944+3442	6.67 ± 0.19	7.66 ± 0.15	6.27 ± 0.11	…
J0944-0038	6.69 ± 0.11	7.83 ± 0.02	6.16 ± 0.02	5.65 ± 0.06
J1024+0524	6.41 ± 0.13	7.80 ± 0.05	6.13 ± 0.01	5.97 ± 0.05
J1025+3622	6.77 ± 0.14	8.13 ± 0.08	6.41 ± 0.03	5.74 ± 0.12
J1044+0353	6.07 ± 0.14	7.55 ± 0.02	5.43 ± 0.01	5.47 ± 0.25
J1105+4444	6.77 ± 0.15	8.23 ± 0.07	6.47 ± 0.02	6.10 ± 0.04
J1119+5130	5.99 ± 0.16	7.59 ± 0.08	5.86 ± 0.05	5.73 ± 0.33
J1129+2034	6.82 ± 0.19	8.30 ± 0.12	6.54 ± 0.01	5.79 ± 0.58
J1132+1411	6.79 ± 0.15	8.24 ± 0.07	6.50 ± 0.02	5.81 ± 0.06
J1132+5722	5.91 ± 0.15	7.34 ± 0.09	5.86 ± 0.05	5.35 ± 0.28
J1144+4012	7.45 ± 0.12	8.65 ± 0.08	…	0.00 ± 0.00
J1148+2546	6.62 ± 0.14	8.01 ± 0.04	6.27 ± 0.01	5.97 ± 0.05
J1150+1501	6.63 ± 0.17	8.14 ± 0.10	6.43 ± 0.01	5.97 ± 0.36
J1225+6109	6.37 ± 0.15	8.02 ± 0.05	6.21 ± 0.02	5.91 ± 0.40
J1253-0312	7.09 ± 0.12	8.02 ± 0.03	6.54 ± 0.01	6.17 ± 0.03
J1314+3452	6.76 ± 0.18	8.27 ± 0.11	6.49 ± 0.01	5.89 ± 0.39
J1359+5726	6.62 ± 0.14	7.99 ± 0.07	6.27 ± 0.02	5.94 ± 0.06
J1416+1223	7.31 ± 0.06	8.15 ± 0.04	6.47 ± 0.11	6.09 ± 0.10
J1418+2102	6.05 ± 0.15	7.51 ± 0.03	5.60 ± 0.00	5.40 ± 0.21
J1444+4237	6.19 ± 0.20	7.38 ± 0.09	…	…
J1448-0110	6.71 ± 0.14	8.07 ± 0.03	6.43 ± 0.01	6.11 ± 0.04
J1521+0759	7.24 ± 0.11	8.67 ± 0.07	7.04 ± 0.25	6.62 ± 0.16
J1545+0858	6.35 ± 0.13	7.75 ± 0.02	6.05 ± 0.00	5.84 ± 0.20

Note. N/H, O/H, and S/H are compiled from Paper XII, Paper IV, and Paper IV, respectfully, while Fe/H is from this work.

2017). These results suggest that feedback and dust processing regulate the apparent Fe abundance in starburst environments, delaying the return of Fe to the gas phase until grains are destroyed and metals are fully mixed.

6.1.3. Nitrogen

A rather different distribution is seen for N in Figure 4(a), with $N/H_{\rm ion.}$ being consistently higher than $N/H_{\rm neu.}$.

The mean $\rm ICF_{tot.}$ value for $N/H_{\rm neu.}$ is ∼0.05, which is far smaller than the average offset between the two phases of $\langle \Delta N/H \rangle = -0.70 \pm 0.38$. N is mostly produced in intermediate-mass AGB stars (4–7 $M_\odot$, over >100 Myr timescales; C. Kobayashi et al. 2011), with a small portion produced in Type II SNe (C. Kobayashi et al. 2020). W-R stars can also be a primary source of nitrogen production in galaxies over ∼3–5 Myr timescales.

W-R stars are massive stars that have shed their outer hydrogen layers, exposing a helium core enriched with nitrogen created as a byproduct of the CNO cycle. This nitrogen is then expelled into the surrounding ISM via strong stellar winds, significantly contributing to the overall nitrogen abundance in a galaxy. While W-R features have been definitively detected in only four CLASSY galaxies (J0127 −0619, J1129+2034, J1157+3220, and J1225+6109), and may remain undetected in the other low-metallicity systems due to the weakness of the spectral signature, W-R stars can still be a source of significant N enrichment due to the timescales involved with chemical mixing.

We further explore factors that may contribute to the offset in nitrogen abundance in Section 7.2.

6.2. Multiphase Abundance Ratios: N/O, S/O, and α/Fe

Different elements are created as part of different nucleosynthetic processes and in stars with different stellar masses, on different timescales. As such, assessing trends in elemental abundances relative to O will be a direct result of how different elements are synthesized in stars and therefore provide clues about the age and metallicity of the stellar population that has enriched the interstellar gas. In particular, comparing the abundance ratio within the ionized and neutral phases of the gas can be a powerful tool to understand if/how the nucleosynthesis yields (which begin mixing in the ionized gas) are also echoed in the neutral gas (provided that dust affects the neutral and ionized-gas phases in a similar manner). In Figures 5(a)–(d) we show the neutral and ionized-gas abundances of N/O, S/O, O/Fe, and S/Fe within that specific phase as a function of the ionized-phase metallicity.

6.2.1. N/O versus O/H

Nitrogen is nucleosynthetically produced as a byproduct of the CNO cycle, which consumes carbon and oxygen as catalysts. At low metallicities, there is very little C and O in the gas from which stars form, and so only stars massive enough to produce their own seed C and O can trigger N production via the CNO cycle. Because this production only depends on the initial H and He within the star, the production of N/O is metallicity independent, or *primary*. At higher metallicities, the initial C and O can sufficiently seed the CNO cycle such that N/O increases with increasing O/H. Further, N and O are produced and released by stars of different masses, on different timescales, essentially behaving as a chemical-evolutionary "clock" (e.g., L. van Zee & M. Haynes 2006; E. Pérez-Montero et al. 2013; D. A. Berg et al. 2019, and references therein) of recent star formation. The complexity of the N/O–O/H relationship lies in the fact that N can be produced in both massive stars ($M > 8M_\odot$) and intermediate-mass stars (e.g., AGB stars; C. Kobayashi et al. 2011). In the latter, N may not be released until up to >100 Myr (C. Kobayashi et al. 2020), which is a significant delay compared to O being released by Type II SNe after ∼10–40 Myr.

Paper XII showed that CLASSY galaxies follow the canonical N/O–OH relationship for the ionized gas. At low metallicities, N/O remains fairly constant at $-1.5 < \log(N/O) < -1.0$, consistent with the plateau seen in other ionized-gas samples (log (N/O)∼−1.4; e.g., D. A. Berg et al. 2019). However, at 12+log (O/H)∼8, CLASSY shows a large scatter in log(N/O) of up to 1.5 dex, which Paper XII attributes to a combination of density, star formation, and outflows tracing different gas conditions.

Interestingly, as we now compare with the neutral gas, in Figure 5(a) we can see a distinct offset between the two phases, with $\langle N/O_{\rm ion.} \rangle = -1.34 \pm 0.25$ and $\langle N/O_{\rm neu.} \rangle = -2.07 \pm 0.38$. Since there is a good agreement between $O/H_{\rm ion.}$ and $O/H_{\rm neu.}$ (Figure 5), the process that produces more N in the ionized gas needs to be on shorter timescales than the release of O by SNe II. Instead, it confirms that the higher levels of N/H in the ionized gas relative to the neutral must be related to other processes, which we explore in

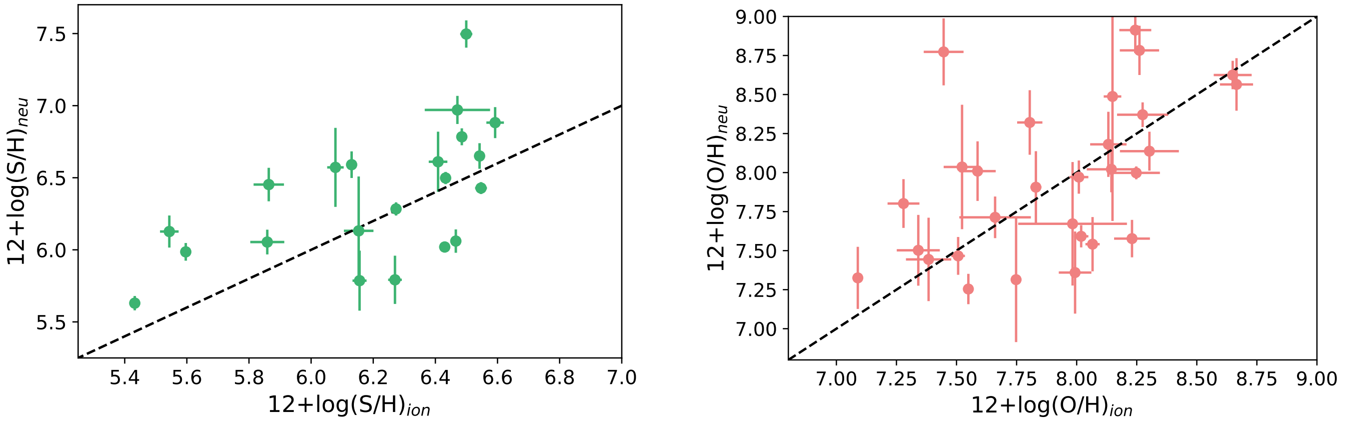

(a) Sulfur **(b) Oxygen**

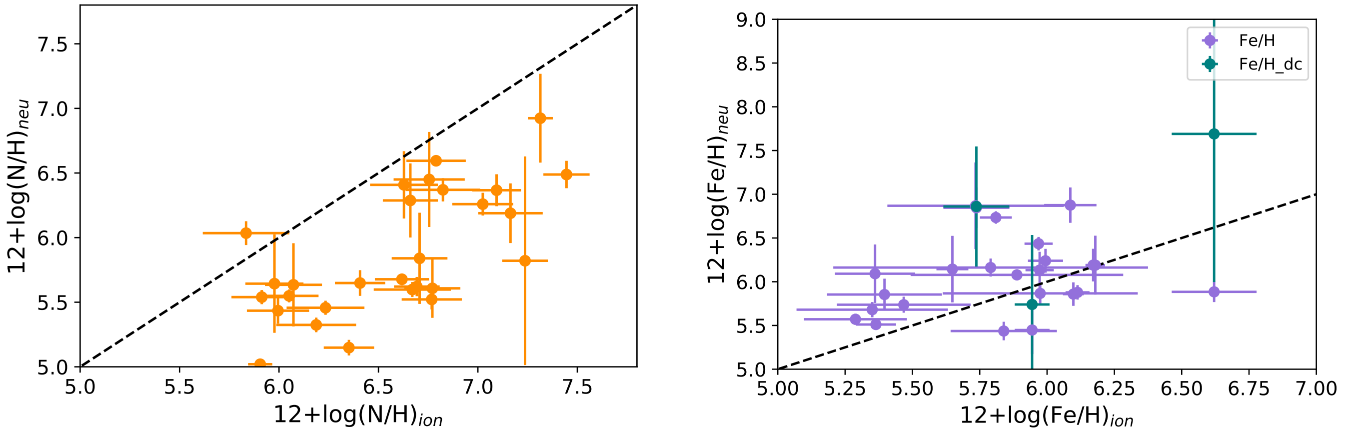

(c) Nitrogen **(d) Iron**

Figure 4. Ionized vs. neutral-gas abundances, with a 1:1 ratio overlaid (black dashed line). Both neutral- and ionized-gas abundances are ICF-corrected, as detailed in Sections 4.1 and 5. For neutral-gas Fe, we include both Fe/H$_{\rm neu}$ and the depletion-corrected values (Fe/H$_{dc}$) for comparison.

Section 7. In particular, here we can see that while the typical "N/O plateau" is seen in the ionized gas (Paper XII), the plateau in the neutral gas appears to have a much larger dispersion (σ(N/O)$_{\rm neu.}$ = 0.38), which could be a reflection on the different levels of enrichment experienced by previous star formation episodes in these systems.

6.2.2. S/O versus O/H

While both S and O are created as part of the α–capture process, S also has contributions from Type 1a SNe (F. Matteucci & C. Chiappini 2005). In Figure 5(b), we show the S/O values for the neutral and ionized gas as a function of metallicity. For both phases, the S/O values are aligned with the solar value, with averages of $\langle$S/O$_{\rm ion.}\rangle$ = –1.71 ± 0.16 and $\langle$S/O$_{\rm neu.}\rangle$ = –1.58 ± 0.15 for the ionized and neutral phases, respectively. The fact that O and S abundances for the neutral and ionized-gas abundances scale in sync with one another suggests that the Type 1a contribution to S enrichment may be negligible in CLASSY galaxies, or yet to be seen since the ages of the current starbursts are all <1 Gyr (see Appendix B).

6.2.3. α/Fe versus O/H

Iron is predominantly produced in Type Ia SNe (>70%), with smaller contributions from Type II SNe and AGB stars (F. Matteucci 2012; C. Kobayashi et al. 2020). Consequently, Fe enrichment occurs over long timescales (~1 Gyr), whereas α-elements such as O and S are injected into the ISM rapidly, on ~5–10 Myr timescales. The α/Fe abundance ratio therefore provides insight into a galaxy's star formation history and chemical evolution, with higher α/Fe indicating shorter/more recent star formation timescales, typically observed in young galaxies or outer regions of galaxies (E. Tolstoy et al. 2009; C. Kobayashi et al. 2020; A. Velichko et al. 2024). This arises because α-elements are primarily produced in the early stages of a star formation episode and are more prevalent in low-metallicity environments, whereas Fe accumulates later, particularly from Type Ia SNe in more evolved populations.

In Figures 5(c) and (d), we show O/Fe and S/Fe for the neutral and ionized gas as a function of the ionized-gas metallicity ([O/H]). Both phases exhibit supersolar ratios: $\langle$O/Fe$_{\rm neu.}\rangle$ = 1.81 ± 0.38, $\langle$O/Fe$_{\rm ion.}\rangle$ = 1.97 ± 0.22; $\langle$S/Fe$_{\rm neu.}\rangle$ = 0.18 ± 0.33, $\langle$S/Fe$_{\rm ion.}\rangle$ = 0.33 ± 0.22. These elevated α/Fe ratios are consistent with the starburst-dominated, UV-bright, nature of CLASSY galaxies (Paper I). The similarity between the neutral and ionized phases suggests that both retain the imprint of previous star formation episodes older than ~1 Gyr, allowing sufficient time for Type Ia SNe to enrich Fe. This also signifies that any α-enriched material from the most recent starburst has not had sufficient time to fully

Table 6

Offset between Neutral and Ionized-gas Abundances, where $\Delta X/H = \log(X/H_{neu}) - \log(X/H_{ion})$

Target	ΔN/H	ΔO/H	ΔS/H	ΔFe/H
J0127-0619	−0.59 ± 0.32	0.29 ± 0.41	0.27 ± 0.28	…
J0144+0453	0.20 ± 0.24	1.33 ± 0.23	…	…
J0337-0502	−0.89 ± 0.06	−0.62 ± 0.15	−0.28 ± 0.03	0.15 ± 0.08
J0405-3648	−0.33 ± 0.41	0.52 ± 0.17	0.58 ± 0.12	0.73 ± 0.37
J0823+2806	< -0.50	−0.25 ± 0.11	−0.12 ± 0.05	0.01 ± 0.34
J0934+5514	…	0.24 ± 0.20	…	0.28 ± 0.20
J0938+5428	−0.77 ± 0.18	0.52 ± 0.18	0.29 ± 0.11	0.25 ± 0.15
J0940+2935	−0.78 ± 0.20	−0.31 ± 0.46	−0.02 ± 0.38	…
J0944+3442	−1.07 ± 0.20	0.05 ± 0.20	…	…
J0944-0038	−1.07 ± 0.14	0.08 ± 0.23	−0.37 ± 0.21	0.50 ± 0.38
J1024+0524	−0.62 ± 0.18	0.52 ± 0.21	0.46 ± 0.09	−0.41 ± 0.17
J1025+3622	−1.16 ± 0.27	0.05 ± 0.22	0.20 ± 0.21	1.11 ± 0.26
J1044+0353	−0.45 ± 0.56	−0.31 ± 0.63	0.19 ± 0.44	0.26 ± 0.51
J1105+4444	−1.29 ± 0.19	−0.69 ± 0.19	−0.45 ± 0.12	−0.28 ± 0.16
J1119+5130	−0.56 ± 0.19	0.42 ± 0.21	0.59 ± 0.13	1.13 ± 0.59
J1129+2034	−0.45 ± 0.21	−0.17 ± 0.17	0.11 ± 0.09	0.37 ± 0.59
J1132+1411	−0.20 ± 0.15	0.67 ± 0.16	1.00 ± 0.10	0.92 ± 0.09
J1132+5722	−0.37 ± 0.16	0.16 ± 0.24	0.19 ± 0.10	0.33 ± 0.29
J1144+4012	−0.96 ± 0.16	−0.02 ± 0.12	…	…
J1148+2546	−0.94 ± 0.14	−0.04 ± 0.11	0.01 ± 0.05	0.47 ± 0.09
J1150+1501	−0.22 ± 0.31	−0.12 ± 0.18	0.07 ± 0.04	−0.11 ± 0.38
J1225+6109	−0.36 ± 0.27	−0.30 ± 0.16	−0.02 ± 0.05	0.02 ± 0.41
J1253-0312	−0.73 ± 1.19	−0.43 ± 0.08	…	0.02 ± 0.19
J1314+3452	−0.50 ± 0.18	0.07 ± 0.13	0.25 ± 0.04	0.19 ± 0.40
J1359+5726	…	−0.62 ± 0.49	−0.44 ± 0.42	−0.52 ± 0.31
J1416+1223	−0.39 ± 3.45	0.34 ± 0.80	0.50 ± 0.14	0.79 ± 0.22
J1418+2102	−0.50 ± 0.16	−0.04 ± 0.12	0.39 ± 0.06	0.46 ± 0.28
J1444+4237	−0.86 ± 0.21	0.06 ± 0.28	…	…
J1448-0110	−0.96 ± 0.15	−0.52 ± 0.18	−0.41 ± 0.04	−0.23 ± 0.09
J1521+0759	−1.42 ± 0.82	−0.10 ± 0.18	…	−0.74 ± 0.20
J1545+0858	−1.20 ± 0.14	−0.43 ± 0.40	…	−0.40 ± 0.22

mix into either phase. The small dispersion between the neutral and ionized phases, together with the age-dependent abundance offsets discussed in Section 7.1.6, indicates that any rapid, galaxy-wide mixing of recently produced α-elements is limited.

Comparisons to other studies reinforce this interpretation. For example, A. Velichko et al. (2024) analyzed α/Fe in 110 DLAs, identifying a high-α plateau ([α/Fe] ~ 0.38) followed by an α-knee at [M/H] ~ -1, corresponding to the onset of significant Type Ia Fe enrichment. CLASSY systems show a somewhat higher plateau for S/Fe ($\sim$0.66 relative to solar, with $\langle S/Fe \rangle \sim 0.28$ for the two phases and $\log(S/Fe)_\odot = -0.38$), likely reflecting top-heavy IMFs and high star formation efficiencies that enhance early α-element production. As with DLAs, lower-mass, low-metallicity galaxies tend to reach the α-knee at lower metallicities; given the low-mass, low-metallicity nature of CLASSY, we would similarly expect an α-knee around [O/H] ~ -1. However, the diverse star formation histories and ages in our sample introduce substantial scatter, preventing a precise determination of the knee location.

7. Discussion

The goal of this study is to understand whether an offset exists between amount of metals locked into the neutral and ionized gas within star-forming galaxies and investigate factors that would contribute to such an offset. To this end, we explore the abundance offsets presented in Section 6 as a function of various galaxy properties, and finally focus on the behavior of nitrogen between gas phases.

7.1. What Controls Gas Mixing between the Phases?

The relative abundances between the neutral and ionized-gas phases trace the efficiency of metal transport and mixing in galaxies. In low-mass systems, feedback from massive stars, SNe, and stellar winds injects newly synthesized elements into the ISM, but the degree to which these metals cool and mix into the neutral phase remains uncertain (M. S. Peeples & F. Shankar 2011; J. Tumlinson et al. 2017). If metals remain confined to the ionized medium, subsequent generations of stars will form from metal-poor gas, delaying chemical enrichment and sustaining large-scale inhomogeneities (A. Emerick et al. 2020; B. L. James et al. 2020; A. De Cia et al. 2021). Conversely, efficient mixing on short timescales would homogenize the ISM and erase phase-dependent differences. To investigate these processes, we examine how the abundance offsets (ΔN/H, ΔO/H, ΔS/H, ΔFe/H) vary with global galaxy properties and internal conditions (Figures 6(a)–(f)). Linear relations were fitted using the `ltsfit` algorithm (M. Cappellari et al. 2013), and correlation strengths were quantified with the Pearson coefficient (r) and significance (p).

7.1.1. Metallicity

Figure 6(a) shows the abundance offsets as a function of ionized-gas metallicity (12+log(O/H)). All four elements (O, N, S, and Fe) show weak decreasing correlations with metallicity ($-0.39 \leqslant r \leqslant -0.13$). O, S, and Fe exhibit modestly higher neutral-phase abundances at low metallicities (12+log(O/H)$\lesssim$8.25), whereas N is offset by roughly

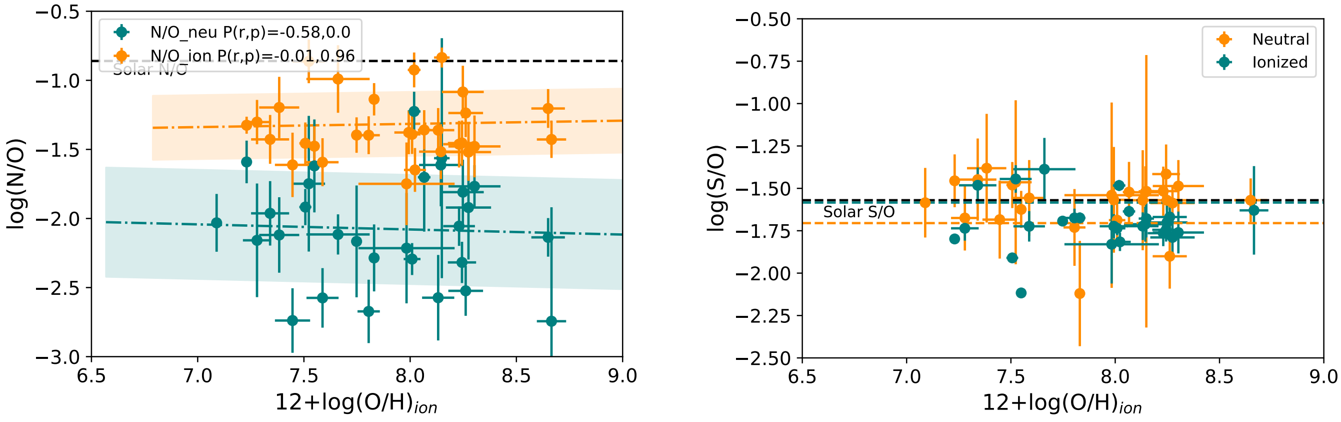

(a) N/O (b) S/O

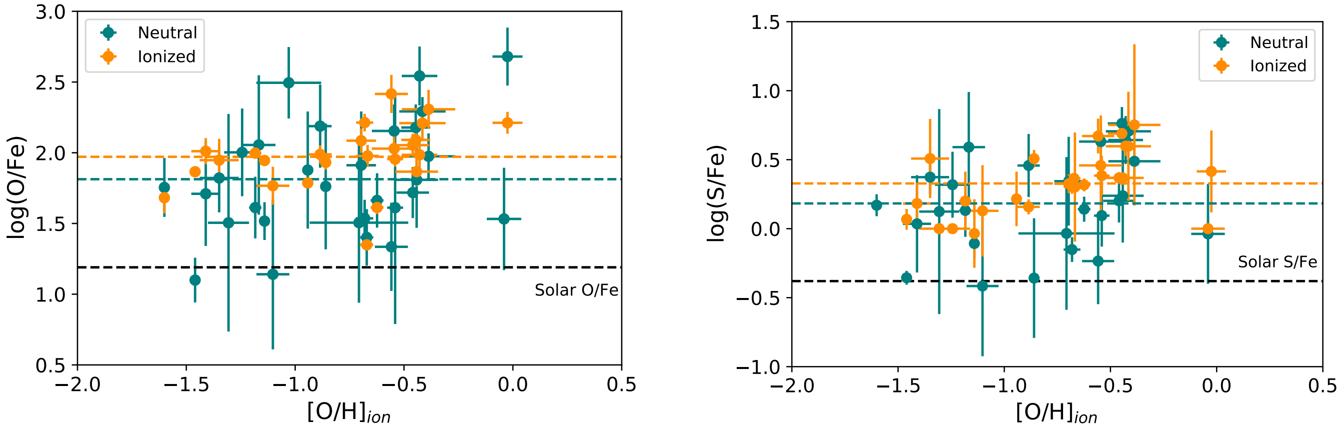

(c) O/Fe (d) S/Fe

Figure 5. Abundance ratios for both the ionized and neutral gas as a function of the metallicity (i.e., oxygen abundance of the ionized gas). In the bottom two panels, the *x*-axis shows metallicity relative to solar, $[O/H] = \log(O/H) - \log(O/H)_{\odot}$. In each panel, we show the respective solar ratio value as a black dashed line, with the average values as orange and teal dashed lines for the ionized and neutral gas, respectively.

1 dex lower than the other elements, indicating consistently higher ionized-phase abundances. This trend is surprising, as no significant connection is expected between the amount of metals in a galaxy and relative distribution of metals between the neutral and ionized phases. However, the production mechanisms of the elements considered here may play a role.

High N/O in the ionized phase has been proposed to result from low effective yields of oxygen, where α–elements are preferentially ejected from ionized regions via CCSNe (or SNe II; e.g., D. A. Berg et al. 2019). Such events inject large amounts of O, S, and Fe into hot, metal-rich outflows that may escape low-mass galaxies or remain in the CGM (e.g., M.-M. Mac Low & A. Ferrara 1999; S. Recchi et al. 2008; A. Emerick et al. 2018), temporarily depleting these elements from the warm ISM. In contrast, nitrogen released by slower, less energetic sources such as AGB stars and W-R winds is more readily retained, as these stars are longer-lived, more spatially dispersed, and deposit their material into denser, cooler regions where mixing is efficient. This differential retention naturally leads to an enhancement of N/O in the ionized phase.

7.1.2. Stellar Mass

Galaxy mass can influence metal retention and mixing. Dwarf galaxies retain only ∼5%–10% of their metals in the ISM and stars (K. B. W. McQuinn et al. 2015), but whether the neutral and ionized phases are affected differently is unclear. Outflow properties derived from emission and absorption lines (Si II, Si III, Si IV) suggest that broad components trace the same outflowing gas (X. Xu et al. 2024), implying similar retention in both phases. Stellar mass estimates from Paper I (Figure 6(b)) show little correlation with abundance offsets ($P(p) > 0.13$), suggesting that mass has little effect on metal mixing between the phases.

7.1.3. Star Formation Rate

Feedback from massive stars can eject metals into the ionized medium and affect the relative abundances between phases (e.g., P. F. Hopkins et al. 2019; M. C. Jecmen & M. S. Oey 2023). Figure 6(c) shows abundance offsets as a function of SFR. While O, S, and Fe show moderate, nonsignificant trends ($P(p) = 0.12$–0.19), nitrogen exhibits a strong negative correlation ($P(r, p) = -0.46, 0.01$), with higher-SFR systems showing enhanced ionized-phase nitrogen. This likely reflects the short timescales (∼10 Myr) of recent starburst-driven enrichment, consistent with W-R stars as the primary source of N.

For specific SFR (Figure 6(d)), oxygen shows a statistically significant negative correlation ($P(r, p) = -0.47, 0.01$), consistent with enhanced Type II SNe enrichment in high-

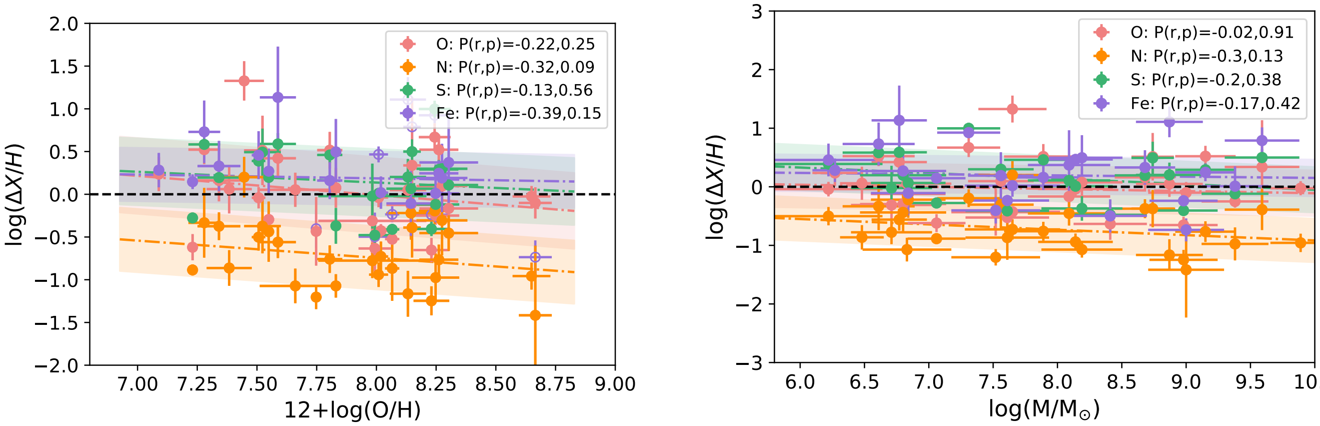

(a) $\Delta X/H$ vs. metallicity **(b) $\Delta X/H$ vs. stellar mass**

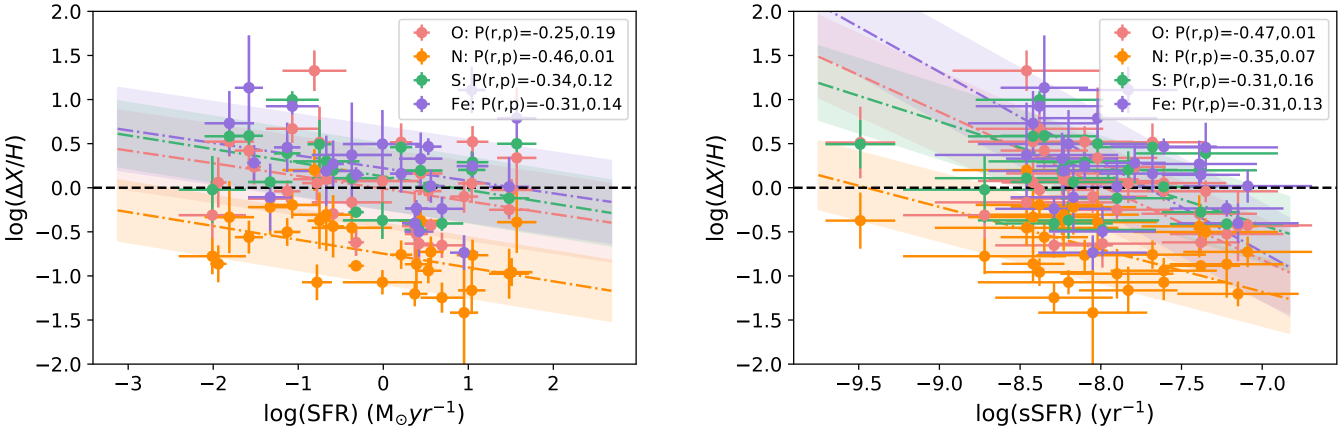

(c) $\Delta X/H$ vs. star-formation rate **(d) $\Delta X/H$ vs. specific star-formation rate (sSFR)**

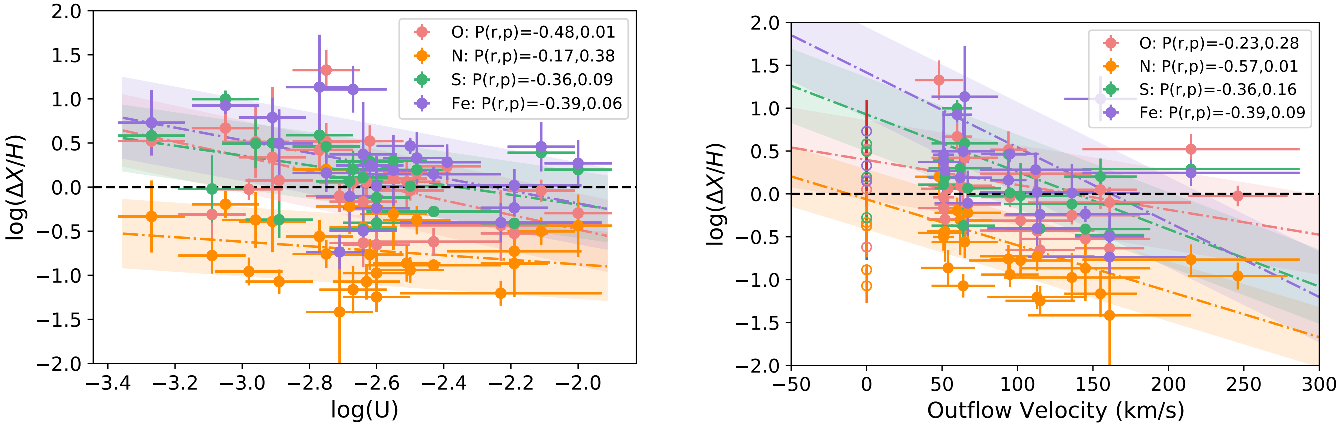

(e) $\Delta X/H$ vs. ionization parameter **(f) $\Delta X/H$ vs. ISM outflow velocity (V_{out})**

Figure 6. Neutral–ionized-gas abundance offset (ΔX/H) as a function of different galaxy properties, where ΔX/H = X/H$_{\rm neutral}$ − X/H$_{\rm ionized}$, such that a positive Δ(X/H) implies a higher abundance of X in the neutral gas. The Pearson correlation coefficients for each linear fit are provided in the plot legend. Open circles in panel (f) denote galaxies with no detected outflow and are not included in the linear fit.

sSFR systems. S and Fe follow similar, weaker trends, indicating that starburst intensity modulates the relative enrichment of ionized gas.

7.1.4. Ionization Parameter

The ionization parameter (U, derived in Paper IV) traces the strength of the radiation field and the relative ionization state of the gas. Figure 6(e) shows that higher log(U) correlates with smaller abundance offsets, especially for oxygen ($P(r, p)$ = –0.48, 0.01), consistent with harder radiation fields driving a larger fraction of metals into the ionized phase. Correlations are weaker for N ($P(r, p)$ = –0.17, 0.38) and moderate for Fe ($P(r, p)$ = –0.39, 0.06) and S ($P(r, p)$ = –0.36, 0.09), reflecting differences in ionization potentials and depletion.

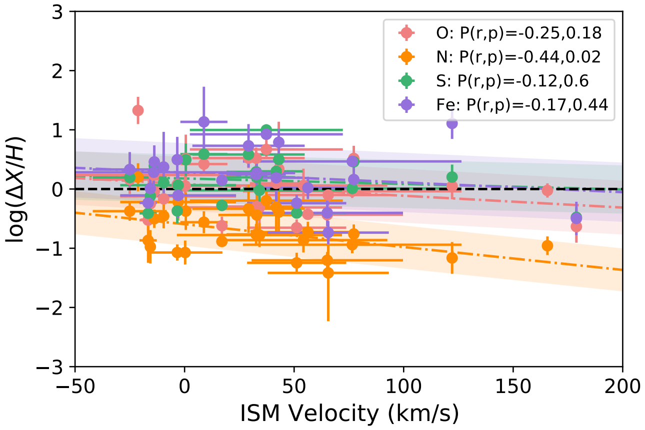

Figure 7. $\Delta X/H$ as a function of the ISM velocity ($V_{\min}$) derived by Paper XI.

7.1.5. Gas Kinematics

Outflows and ISM velocities can affect metal mixing. Figure 6(f) shows abundance offsets versus outflow velocity (v_{out}) measured from the broad component of the Si II absorption lines in Paper III. All elements show a negative trend with outflow velocity, although only for nitrogen is this correlation highly statistically significant: faster ISM velocities correspond to higher ionized-phase N/H. For elements such as N, O, and S, which are predominantly produced by massive stars, these trends are consistent with enrichment driven by stellar feedback and outflows, and the observed abundance patterns in the ionized gas reflect the expected signature of recent massive-star activity. Figure 7 shows similar trends using the average ISM velocity ($v_{\min}$) derived from the centroid of the main, narrow ISM component of the absorption-line fits. These results indicate that nitrogen enrichment is particularly sensitive to gas kinematics, likely because outflows delay mixing of W-R-ejected material with the neutral phase, which we discuss further in Section 7.2.

7.1.6. Stellar Population Age

Stellar population age strongly influences element release and mixing timescales. In this context, UV-based mass-weighted ages are particularly useful, as they sample both the young burst populations responsible for rapid W-R and Type II SNe enrichment and older populations where metals have equilibrated between phases. By comparison, UV light-weighted ages trace only the most recent burst, while optical ages sample only older Gyr populations (as detailed in Appendix B and shown in Table 10). Utilizing UV mass-weighted ages, Figure 8 shows complex trends: offsets decrease from positive to negative until ∼5–8 Myr, rise sharply by ∼1 dex, then decline gradually, stabilizing by ∼20 Myr. Each element required a bimodal linear fit separating "young" (<5–8 Myr) and "old" (>5–10 Myr) populations. The correlation is strongest in young populations ($P(p) = 0.01$–0.18) and weaker in older ones, particularly for N and Fe ($P(p) = 0.33, 0.73$).

All elements except nitrogen show early ionized-phase enhancements due to Type II SNe, followed by cooling and mixing that equilibrates O, S, and Fe by ∼20–30 Myr. Nitrogen remains overabundant in the ionized gas, peaking within ∼10 Myr, consistent with W-R star yields (R. B. C. Henry et al. 2000). We also indicate which systems are classified as "multiburst" (J. e. a. Parker 2025, in preparation, hereafter Paper XIII), whose stellar continua were best fit with multiple bursts separated by >20 Myr. These correspond to older populations where $\Delta X/H{\sim}0$, confirming that sufficient time allows metals to homogenize between phases for S, O, and Fe, but not N.

Overall, the analysis of abundance offsets reveals a complex, element-dependent picture of chemical mixing in low-mass star-forming galaxies. Oxygen, sulfur, and iron are generally well mixed across all systems, with modest ionized-phase enhancements in galaxies with higher sSFRs, harder radiation fields, or younger stellar populations, reflecting prompt enrichment from Type II SNe and rapid SN-driven turbulent mixing. Nitrogen, in contrast, consistently exhibits higher abundances in the ionized gas, with strong dependencies on metallicity, SFR, sSFR, ionization parameter, stellar age, and outflow velocity. The UV-based mass-weighted stellar ages provide a particularly powerful diagnostic, sampling both the recent starburst populations responsible for W-R-driven nitrogen enrichment and the older stellar populations where metals have equilibrated between phases. Multiburst systems Paper XIII show $\Delta X/H{\sim}0$, confirming that sufficient time and dynamical mixing allow metals to homogenize. These results underscore the importance of both stellar population age and gas dynamics in shaping the phase-dependent chemical structure of low-mass galaxies, and provide a framework for interpreting observed abundance offsets in terms of the timescales of feedback, enrichment, and mixing.

7.2. Why Is Nitrogen Behaving Differently?

As shown in Section 7.1, several global and internal parameters correlate with an enhancement in the amount of nitrogen in the ionized gas relative to the neutral phase. Increasing stellar mass, SFR, outflow velocity, and stellar population age (particularly up to ∼10 Myr) all correspond to a larger ionized-gas offset for N/H. Regardless of the property considered, nitrogen is consistently more abundant in the ionized phase than in the neutral phase, unlike O, S, and Fe. This systematic behavior implies that the production, release, and transport of nitrogen differ fundamentally from those of α- and iron-peak elements in the ISM of star-forming galaxies.

To disentangle the processes controlling this behavior, Figure 9 shows N/H in both the ionized and neutral phases as a function of stellar age. The absolute abundance of nitrogen increases slightly in both phases for <10 Myr, subsequently decreasing slightly for the ionized-gas but strongly for the neutral-gas, indicating that the total amount of nitrogen is not solely governed by the timescale on which it was produced. However, Figure 9 demonstrates that the *relative* abundance, $\Delta(\mathrm{N/H})$, depends strongly on stellar age within the first ∼10 Myr of a burst, implying that the enrichment source itself—rather than the global evolutionary timescale—drives the observed offsets. In other words, the phase differences reflect the immediate chemical imprint of massive-star feedback rather than gradual, global mixing processes. Once galaxies evolve beyond ∼10 Myr, $\Delta(\mathrm{N/H})$ decreases, and the phases approach chemical equilibrium, consistent with the end of the W-R phase and subsequent mixing of the ejecta. We did investigate whether there was a correlation between stellar age and outflow velocity, but found none, suggesting that efficient

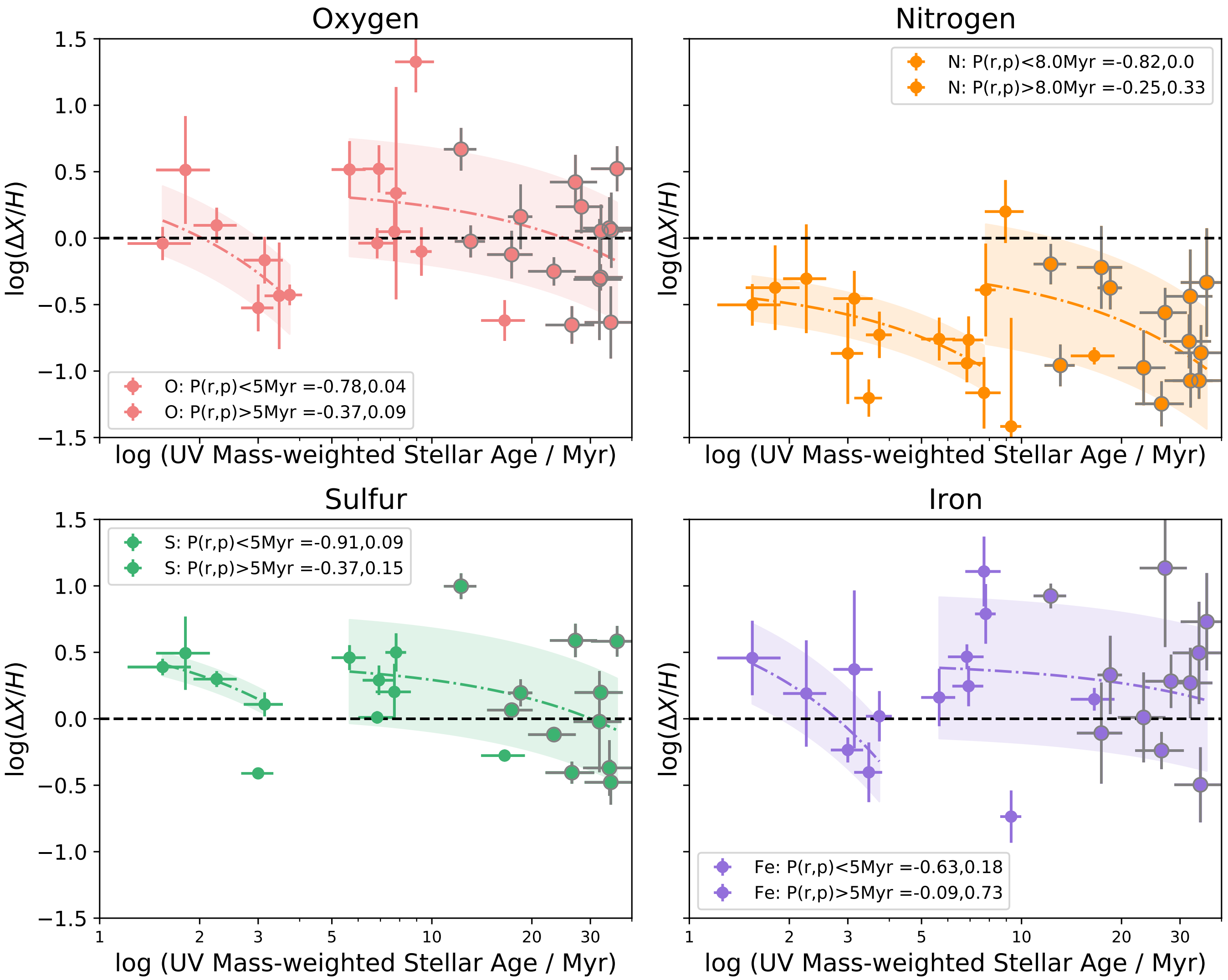

Figure 8. Neutral–ionized-gas abundance offset (ΔX/H) as a function of mass-weighted stellar population age (Section 7.1.6), where $\Delta X/H = X/H_{\mathrm{neu.}} - X/H_{\mathrm{ion.}}$, such that a positive Δ(X/H) implies a higher abundance of X in the neutral gas. Linear regression fits are shown in each panel (dotted–dashed lines and shaded regions), along with the corresponding Pearson correlation coefficients, where piecewise linear fits were performed according to age break-points indicated in the legend. Galaxies classified as multiburst systems by Paper XIII are outlined in gray.

mixing in older systems is not simply the result of weaker feedback.

If W-R stars dominate nitrogen production in these systems, their fast, ionized stellar winds should both enrich and dynamically disturb the surrounding gas. Figure 10(a) shows a strong correlation between both N/H_{ion} and N/H_{neu} with v_{out} ($P(r, p) = 0.68$, 0.01 and 0.44, 0.03, respectively), while the offset ΔN/H exhibits an even stronger dependence (Figure 10(b); see also Figure 6(f)). These trends indicate that the same winds responsible for nitrogen injection also drive the observed ISM kinematics, with higher-velocity systems manifesting a larger fraction of nitrogen in the ionized phase. A similar relationship between v_{out} and N/O was reported by Paper XII, who found more elevated N/O ratios in systems with stronger outflows. In this scenario, nitrogen-rich, high-velocity winds inhibit efficient cooling and mixing with the neutral medium, thereby maintaining the observed phase-dependent abundance offsets.

We further examine the role of feedback strength using the mass-loading factor, η, defined as the ratio of mass outflow rate ($\dot{M}_{\mathrm{out}}$) to SFR, as measured by Paper III. As shown in Figure 11, both ionized and neutral N/H decrease strongly with increasing η ($P(r, p)$ = –0.69, 0.01 and −0.41, 0.06, respectively). If we consider N/H to be a proxy for the overall metal content (and hence mass) of the galaxy, the correlation is consistent with low-mass galaxies exhibiting more efficient outflows. This behavior is in accordance with the findings of Paper XIII, who showed that systems with low η display higher N/O in the ionized gas, implying that inefficient winds allow nitrogen to remain and cool within the ISM. Conversely, large η systems lose a greater fraction of their freshly produced metals, leading to lower overall abundances in both phases. Although one might expect ΔN/H to correlate with η, such a relationship is not observed, indicating that feedback-driven metal loss affects both phases similarly, whereas the persistence of nitrogen in the ionized medium is instead tied to its mode of ejection and ionization structure.

Overall, the data reveal that nitrogen remains overabundant in the ionized gas under all conditions examined. While this could suggest that the cooling and mixing timescales for nitrogen exceed the stellar ages sampled here, Figure 9 demonstrates that the gas becomes chemically well mixed on

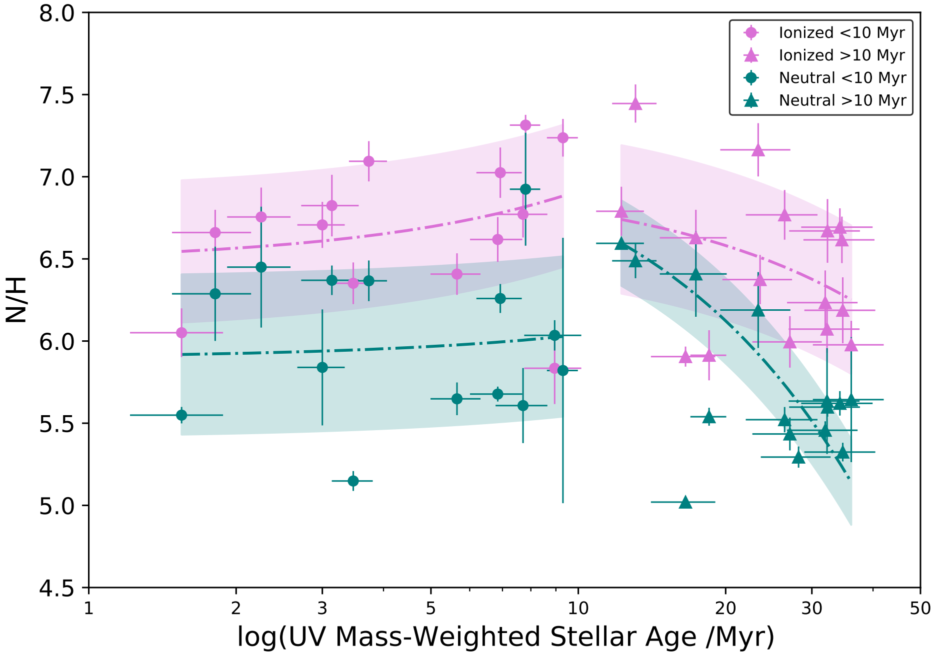

Figure 9. Nitrogen abundances for the neutral and ionized gas as a function of stellar age. Here, we separate the sample at a stellar age of ∼10 Myr to highlight the two-piece correlation with age shown in Figure 8.

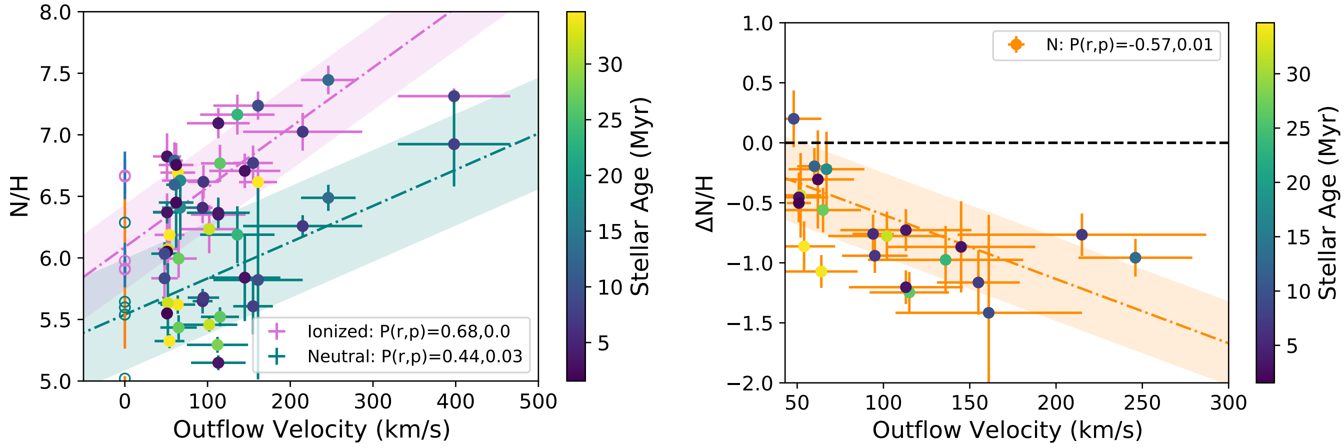

(a) **(b)**

Figure 10. Nitrogen abundances for the neutral and ionized gas as a function of outflow velocity. In panel (a) we show the absolute abundance (N/H) separately for each phase, while in panel (b) we show the difference between the two phases (ΔN/H). Both panels are color-coded by mass-weighted stellar age.

∼10–35 Myr timescales for some systems. The magnitude of ΔN/H increasing with ISM velocity therefore implies that in systems with strong outflows, a portion of the ionized nitrogen may be expelled before cooling and recombining into the neutral phase. The opposite trend with stellar mass—larger offsets in more-massive, metal-rich systems with larger outflow velocities Paper III—may instead reflect ionization-structure effects. Since the ionization potential of N is higher than that of H, a smaller fraction of nitrogen will reside in the neutral state. We note that removing the neutral-phase $\mathrm{ICF_{tot}}$ corrections would increase ΔN/H further, reinforcing that this offset is real and not an artifact of ionization modeling.

To determine whether the observed nitrogen excess arises from recent enrichment or delayed mixing, we examine the N/O ratio in both phases as a function of stellar age (Figure 12). For the youngest systems (<10 Myr), $\mathrm{N/O_{ion}}$ remains approximately constant with age, while $\mathrm{N/O_{neu}}$ decreases significantly ($P(p)$ = –0.67, 0.01) and displays substantial scatter—consistent with freshly ejected, nitrogen-rich material from W-R stars that has not yet mixed into the cooler ISM. At older ages (>10 Myr), $\mathrm{N/O_{ion}}$ stays roughly constant, but $\mathrm{N/O_{neu}}$ rises by nearly 1 dex before gradually declining again with increasing age ($P(p)$ = –0.55, 0.05). The nitrogen seen in the neutral gas represents material expelled during earlier bursts that has cooled and mixed into the ISM, while the ionized phase traces additional N enrichment from W-R stars during the most recent burst over a timescale of ∼3 Myr. Since oxygen from CCSNe is released on longer ∼10 Myr timescales, this introduces a natural time lag in the production and mixing of nitrogen relative to oxygen, which manifests as the evolving N/O ratio across both phases. The evolution of the phase offset Δ(N/O) (Figure 13) supports this scenario: a strong anticorrelation at young ages ($P(p)$ = 0.01) reflects the W-R enrichment phase, after which Δ(N/O)

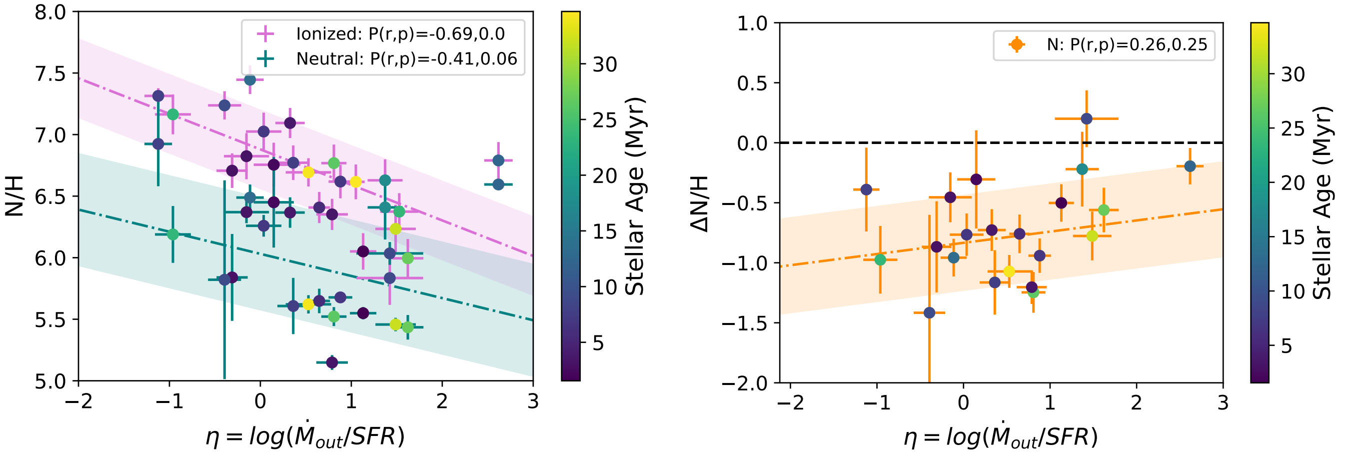

(a)

(b)

Figure 11. Nitrogen abundances for the neutral and ionized gas as a function of mass outflow factor, η. In panel (a) we show the absolute abundance (N/H) separately for each phase, while in panel (b) we show the difference between the two phases (ΔN/H).

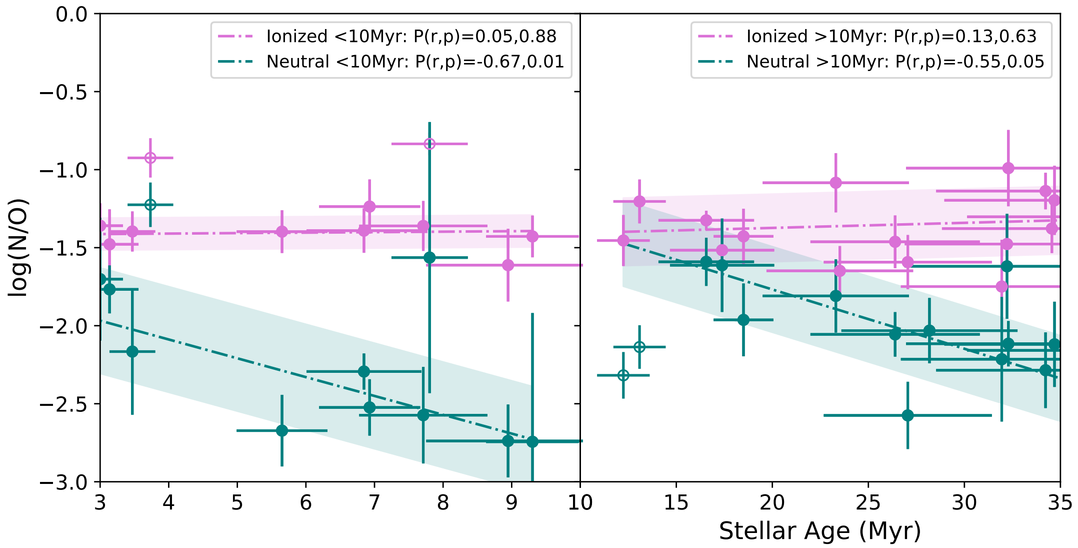

Figure 12. N/O as a function of stellar age. Here we separate the sample at a stellar age of ∼10 Myr to highlight the two-piece correlation with age shown in Figure 8. Linear regression fits are shown in each panel (dotted–dashed lines and shaded regions), along with the corresponding Pearson correlation coefficients, where separate fits were performed on the < 10 Myr and > 10 Myr populations. Empty symbols were removed from the fit via the sigma-clipping algorithm.

increases by ∼1.5 dex as the ISM becomes chemically homogenized, then gradually declines as mixing continues on longer timescales.

A remaining puzzle is that only four CLASSY galaxies exhibit detectable W-R spectral features, despite the nitrogen signatures implying W-R-driven enrichment. The discrepancy likely reflects observational and temporal limitations: W-R features are short-lived ($\lesssim$3 Myr) and can be diluted in globally integrated spectra (P. Lagos et al. 2012; B. L. James et al. 2013; N. Kumari et al. 2018). Even after the W-R phase ends, their nitrogen-rich ejecta can persist in the ionized ISM, explaining why the chemical imprint outlasts the direct spectral signature. Alternatively, other prompt enrichment channels, such as rapidly rotating massive stars or binary interactions, could contribute to early nitrogen release, similar to those proposed for high-redshift galaxies.

To summarize, the combined evidence from stellar age, kinematics, and mass loading demonstrates that nitrogen traces feedback-regulated enrichment in the ionized phase. Massive stars rapidly inject nitrogen through stellar winds and subsequent SNe, driving outflows that both enrich and dynamically shape the surrounding ISM. The close link between N/H, outflow velocity, and mass-loading factor suggests that stellar winds—particularly from W-R stars—may play a more significant role in powering galactic outflows than previously thought. Indeed, as noted by N. Murray et al. (2005), winds from massive stars can supply a momentum flux comparable to that of SNe (see also C. Leitherer et al. 1999), supporting the view that stellar winds alone can launch substantial outflows prior to the onset of SNe-driven feedback. While canonical models attribute the bulk of feedback energy to Type II SNe (e.g., T. M. Heckman et al. 2015), our results imply that massive stars dominate the earliest and most chemically influential stages of outflow development. On ∼10 Myr timescales, subsequent mixing redistributes these metals into the neutral phase. Taken together, these findings point to a

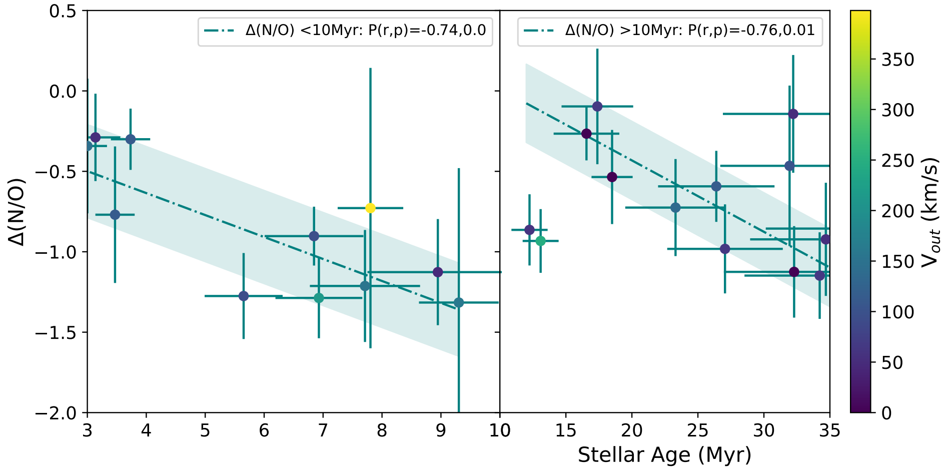

Figure 13. Δ(N/O) (=N/O$_{\rm neu.}$–N/O$_{\rm ion.}$) as a function of stellar population age, color-coded by outflow velocity ($V_{\rm out}$). Here we separate the sample at a stellar age of ~10 Myr to highlight the two-piece correlation with age shown in Figure 8.

more prominent role for stellar winds in regulating both the dynamics and chemical evolution of galaxies—an idea that warrants further exploration through simulations coupling enrichment, feedback, and multiphase gas transport.

7.2.1. N *Enrichment at High-z*

As discussed in Section 7.1, the relationship between stellar population age, ionized outflows, and gas-phase abundances provides a direct window into the cycle of metal enrichment and redistribution. In particular, Figure 10 illustrates how systems with strong outflows and young, burst-dominated stellar populations show elevated N/H in the ionized phase, implying recent nitrogen enrichment by massive stars whose winds have not yet mixed with the cooler gas. These local signatures of feedback-driven N enrichment provide a crucial reference point for interpreting the "nitrogen-loud" galaxies that JWST is now revealing at high redshift.

Nitrogen is an intriguing element that has become a focus of several recent studies, as JWST is revealing high-z systems with extremely high N/O ratios. The first of these was GNz11, a galaxy at $z \sim 10.6$ with unusually bright rest-frame UV emission lines (A. J. Bunker et al. 2023), showing a level of nitrogen significantly higher than that found in local star-forming galaxies of comparable metallicity ($\log({\rm N/O}) = -0.38$). Several more "nitrogen-loud" galaxies have since been discovered, including CEERS-1019 ($\log({\rm N/O}) = -0.38$; S. L. Finkelstein et al. 2022; M. Tang et al. 2023), GHZ2/GLASS-z12 ($\log({\rm N/O}) = -0.29$; M. Castellano et al. 2024), GN-z9p4 ($\log({\rm N/O}) = -0.59$; D. Schaerer et al. 2024), and RXCJ2248-4431 ($\log({\rm N/O}) = -0.39$; M. W. Topping et al. 2024). How these systems achieved such high N/O ratios within such short evolutionary timescales—only ~440 Myr after the Big Bang in the case of GNz11—is puzzling, challenging theoretical stellar yields and galactic chemical evolution, particularly in the early Universe (see D. Nandal et al. 2024, for a review).

Several explanations have been proposed for the large amount of nitrogen in their ionized gas, including signatures of globular cluster precursors, massive-star winds, runaway stellar collisions, tidal disruption events, or the presence of an active galactic nucleus or accreting black hole (A. J. Cameron et al. 2023; C. Charbonnel et al. 2023; R. Maiolino et al. 2024; P. Senchyna et al. 2024). Chemical-evolution models have also managed to reproduce these high N/O levels via two main pathways: (1) rapid chemical enrichment in a dual-starburst model, where W-R stars dominate during the second burst (C. Kobayashi & A. Ferrara 2024), and (2) the contribution of very massive (~2000 $M_\odot$) Pop III stars with ejecta rich in ^{4}He, ^{1}H, and ^{14}N (D. Nandal et al. 2024). However, spectral signatures of W-R stars have not yet been observed in GNz11 despite strong N IV λλ1483,86, C IV λλ1548,50, and He II λ1640 emission (with a possible broad W-R spectral signature; R. Maiolino et al. 2024). If these features originated from W-R winds, comparable strength should also appear in N IV λ1718 and N V λλ1238,40 (P. Senchyna et al. 2021). In contrast, in the Sunburst Arc ($z = 2.37$), T. E. Rivera-Thorsen et al. (2024) detected clear W-R signatures but concluded that the extreme and rapid nitrogen enrichment ($\log({\rm N/O}) = -0.74$) could not be explained by binary W-R models alone, likely requiring an additional population of very massive stars (VMSs). The link between VMSs ($>100\,M_\odot$) and N-enriched galaxies has also been proposed by J. S. Vink (2024), as such stars contribute to both N enrichment and strong He II emission.

The nitrogen trends observed in CLASSY provide an essential low-redshift analog for understanding these chemical conditions now being uncovered at cosmic dawn. In our nearby starbursts, high N/H ratios in the ionized phase are often associated with the presence of W-R stars—despite the lack of shortly lived W-R spectral features—and their enriched winds, which inject nitrogen into the ISM and drive metal-loaded outflows out of the galactic plane (i.e., beyond the neutral ISM), which delay subsequent mixing with the neutral gas reservoir. This combination of localized stellar feedback and incomplete mixing naturally explains the offsets between ionized and neutral gas metallicities (see Figures 10 and 11), as well as the broad, nitrogen-enriched UV emission components (N IV], N V, He II) observed in both local and high-redshift starbursts (e.g., P. Senchyna et al. 2021; R. Maiolino et al. 2024; T. E. Rivera-Thorsen et al. 2024). Such conditions offer a clear physical pathway for the extreme N/O ratios seen in early galaxies: nitrogen enrichment dominated by W-R winds, combined with inefficient metal retention and mixing in the turbulent ISM of rapidly assembling systems.

If the nitrogen emission in high-z "nitrogen-loud" systems is predominantly nebular, the CLASSY galaxies offer direct low-redshift analogs for understanding their chemical conditions. Our analysis shows that W-R-driven winds in young, burst-dominated systems can enrich the ionized gas in nitrogen while simultaneously driving outflows that expel this material before it can cool and mix with the neutral ISM. In this framework, the extreme N/O ratios observed at high redshift naturally arise from localized, rapid enrichment coupled with inefficient mixing, rather than from delayed chemical evolution. Ionized outflows are known to be widespread at high redshift, with 25%–40% of $3 < z < 9$ galaxies in the JADES survey showing signatures of outflowing gas (S. Carniani et al. 2024); this fraction is likely a lower limit, as the relatively low spectral resolution of current data ($R \sim 1000$) may obscure weaker or narrower wind components. The absence of conclusively detected broad outflows in the nitrogen-loud galaxies may therefore reflect observational limitations rather than intrinsic differences in feedback. Together, these findings suggest that the high N/O levels in early galaxies are best explained by nitrogen-rich material ejected into the ISM by W-R stars within the most recent ∼3–5 Myr starburst, consistent with the dual-burst scenario of C. Kobayashi & A. Ferrara (2024).

The local–high-z connection seen in nitrogen thus provides a unified picture: both regimes trace young, burst-dominated galaxies where stellar feedback and outflow dynamics regulate the pace of chemical mixing. The CLASSY galaxies, with their intense radiation fields, elevated ionization parameters, and fast, metal-rich winds, represent nearby analogs of the rapidly assembling systems now accessible with JWST. Understanding these processes in the local Universe is therefore essential for interpreting the emerging population of nitrogen-loud galaxies at $z > 7$, and for disentangling the roles of stellar yields, feedback-driven gas dynamics, and timescale-dependent mixing in shaping galactic chemical evolution across cosmic time.

8. Conclusions

We have presented a comprehensive multiphase chemical analysis of 31 nearby star-forming galaxies from the CLASSY survey, which serve as analogs of high-redshift systems owing to their low metallicities, compact morphologies, and intense radiation fields. By directly comparing the metal content of the ionized and neutral gas phases using matched UV and optical diagnostics, we quantified how key elements (N, O, S, and Fe) are distributed, mixed, and transported within the ISM, and identified the stellar and galactic conditions that regulate this process.

Neutral-gas abundances were derived from Voigt-profile fits to the UV absorption lines of N I, Fe II, S II, O I, and P II, corrected for ionization and line-of-sight contamination using tailored CLOUDY models. Ionized-gas abundances were taken from Paper IV, Paper IX, and Paper XII, with $\mathrm{Fe/H_{ion.}}$ newly derived here from Fe III. Our combined dataset enables a robust, element-by-element comparison of the ionized and neutral metal reservoirs across a wide dynamic range in mass, metallicity, and SFR. The main results are summarized below.

1. Oxygen and sulfur show consistent abundances between the neutral and ionized phases, indicating efficient large-scale mixing of α-elements produced in short-lived massive stars (CCSNe). The remaining intrinsic scatter in both phases reflects local variations in recent enrichment and regions where metals have not yet fully homogenized, revealing small-scale chemical inhomogeneities in the ISM that have not yet mixed on ∼10 Myr timescales.
2. Iron is modestly higher in the neutral phase, even without a full correction for dust depletion, which remains constrained only as a lower limit for all but three galaxies. This likely reflects a combination of enrichment from previous star formation episodes—since Fe from Type Ia SNe requires ∼1,Gyr to accumulate and mix into the cooler ISM—and preferential depletion of Fe onto dust in the ionized phase, where CCSNe shocks can efficiently lock Fe into grains.
3. Nitrogen exhibits the largest phase offset, with $\mathrm{N/H_{ion.}}$ systematically higher than $\mathrm{N/H_{neu.}}$ by ∼0.7 dex in 35/36 systems. The ionized enhancement is consistent with fresh nitrogen from W-R stars and massive-star winds on ∼3–5 Myr timescales, prior to cooling and mixing with the neutral gas.
4. While $\mathrm{N/O_{ion.}}$ lies on the canonical low-metallicity plateau, $\mathrm{N/O_{neu.}}$ is systematically lower, driving an average offset of ∼0.8 dex. In contrast, S/O ratios agree between phases, consistent with their shared nucleosynthetic origin. Both O/Fe and S/Fe ratios are supersolar (∼0.7 dex) and consistent between phases, reflecting α-enhanced enrichment from recent bursts of star formation.
5. The abundance offsets $\Delta(\mathrm{X/H}) = \mathrm{X/H_{neu.}} - \mathrm{X/H_{ion.}}$ correlate most strongly with stellar population age and gas kinematics. Within ∼10 Myr of a burst, the ionized gas becomes progressively enriched in O, S, and Fe produced by CCSNe relative to the neutral medium, after which these elements begin to cool and mix. In contrast, Fe from Type Ia SNe, released on ∼1 Gyr timescales, contributes to the gradual enrichment of the neutral phase. Nitrogen behaves differently: $\Delta(\mathrm{N/H})$ depends most strongly on outflow velocity, implying that stellar feedback regulates whether newly produced nitrogen remains trapped in the ionized phase.
6. The nitrogen behavior in CLASSY mirrors the "nitrogen-loud" galaxies recently uncovered by JWST at $z > 7$. If the high-z N emission is predominantly nebular, our results indicate that W-R-driven winds eject nitrogen straight from the ionized gas, bypassing the neutral phase and delaying mixing. CLASSY galaxies thus provide vital low-z analogs for interpreting these extreme early chemical signatures.

In summary, this work demonstrates that UV absorption-line spectroscopy provides a uniquely powerful probe of the chemical coupling between different ISM phases. By linking multiphase abundances to stellar population age, feedback strength, and gas dynamics, we show that the efficiency of metal mixing varies strongly over ∼10 Myr timescales and depends on both the source and the transport mechanism of enriched material. The tight connection between nitrogen enrichment and outflow strength implies that massive stars, not just SNe, play a central role in powering and chemically shaping galactic winds, motivating future theoretical and observational efforts to quantify their role in driving early outflows. Future UV-capable observatories such as the Habitable Worlds Observatory will be essential for extending such multiphase studies to statistically significant samples across cosmic time, thereby unveiling how feedback, outflows, and star formation jointly govern the chemical evolution of galaxies.

Acknowledgments

B.L.J., M.M., and S.H. are thankful for support from the European Space Agency (ESA). D.A.B. is grateful for the support for this program, HST-GO-15840 provided by NASA through a grant from the Space Telescope Science Institute, which is operated by the Associations of Universities for Research in Astronomy, Incorporated, under NASA contract NAS5-26555. We acknowledge the insightful discussions with Annalisa De Cia in conducting depletion corrections. K.Z.A.C. acknowledges support from a UKRI Frontier Research Guarantee Grant (PI Cullen; grant reference: EP/X021025/1). C.K. acknowledges funding from the UK Science and Technology Facility Council through grant ST/Y001443/1.

Appendix A
Ionization Correction Factors

In this appendix section, we describe the derivation of neutral-gas ICFs, which are used to accurately determine the abundance of metals in the neutral ISM gas, the ionization state of the gas along the line of sight, as described in Section 4.1. The neutral-gas ICFs only apply to the column-density measurements described in Section 3 and should not be confused with ICFs used in ionized-gas chemical abundance measurements (described in Section 5).

Neutral-phase ICFs ($\mathrm{ICF_{neu.}}$) account for unseen higher-ionization states of metal ions that coincide with the H^0–dominated gas by adding the estimated column density of ions like X^{i+1} to the observed dominant state X^i. In practice, they correct the final abundance of the neutral gas by assuming $N(\mathrm{X}) = \mathrm{N}(\mathrm{X}^i) + \sum_{j>0} N(\mathrm{X}^{i+j})$, where $\sum_{j>0} N(\mathrm{X}^{i+j})$ represents the species that are present in the neutral region but cannot be directly measured.

An $\mathrm{ICF_{neu.}}$ can be found by comparing the relative amount of $N(\mathrm{X}^i)$ with $N(\mathrm{X}^{i+1})$ (Figure 2). Most of the elements within the neutral gas of galaxies with $N_{\mathrm{HI}} > 10^{19}$ cm^{-2} are either in the neutral (e.g., Si I) or singly ionized (e.g., Si II) phase. As such, the correction required to account for elements in higher-ionization states (e.g., Si III) is relatively small. However, for N I, accounting for higher-ionization species within the neutral gas (i.e., N II, as it lacks a strong transition in the UV) is essential and can be up to 0.6 dex at high values of N_{HI} (S. Hernandez et al. 2020).

In addition to the neutral-phase ICF, we apply a second correction, $\mathrm{ICF_{ion.}}$ to remove the contribution of the dominant ionization state $N(\mathrm{X}^i)$ that resides in ionized gas along the line of sight. Although H II regions are often approximated as stratified or shell-like, the thickness of each ionic layer varies with excitation energy (see Figure 2). As a result, while the neutral and ionized phases can be cleanly separated using hydrogen, a nonnegligible fraction of the dominant metal ion in the neutral phase is still present in ionized hydrogen gas [$N(\mathrm{X}^i)_{\mathrm{HII}}$]. This contribution must be subtracted from the total column density attributed to the neutral hydrogen dominated regions [$N(\mathrm{X}^i)_{\mathrm{HI}}$] For example, Si II (IP = 16.34 eV) arises in both neutral and ionized-gas regions. While it is predominantly

Table 7
Input Parameters for Ad Hoc CLOUDY Models Used to Derive the ICFs Shown in Table 9 and Discussed in Section 4.1

Target	log[N(Fe III)/N(Fe II)]	Z	F_{1500}/erg s^{-1} cm^{-2} Å^{-1}	L_{UV}/erg s^{-1}	log[N(H I)/cm^{-2}]
J0127-0619	−0.27	0.10	4.04	2.56E+38	21.21
J0144+0453	−0.27	0.12	1.87	1.18E+38	20.18
J0337-0502	−1.08	0.06	7.99	3.22E+39	21.81
J0405-3648	−0.27	0.02	0.96	1.39E+37	20.80
J0823+2806	−1.11	0.39	3.85	2.01E+40	21.61
J0934+5514	0.15	0.02	15.10	2.60E+38	21.24
J0938+5428	−0.27	0.36	3.56	9.41E+40	20.34
J0940+2935	−0.27	0.09	1.45	1.11E+37	21.26
J0944-0038	−0.27	0.14	1.40	7.39E+37	21.67
J0944+3442	0.65	0.09	0.69	6.25E+38	21.51
J1024+0524	0.11	0.14	4.50	1.13E+40	20.58
J1025+3622	−0.97	0.28	1.81	7.59E+40	20.69
J1044+0353	−1.23	0.06	1.70	6.15E+38	21.84
J1105+4444	−0.73	0.35	4.68	4.84E+39	21.87
J1119+5130	−0.27	0.08	2.63	1.26E+38	20.77
J1129+2034	−0.27	0.39	1.87	9.87E+37	21.11
J1132+5722	−0.27	0.08	2.57	1.63E+38	21.24
J1132+1411	−0.16	0.36	1.75	1.21E+39	20.53
J1144+4012	−0.65	0.55	1.20	5.07E+40	20.52
J1148+2546	−0.75	0.18	2.07	9.81E+39	21.19
J1150+1501	−0.27	0.28	12.60	1.82E+38	21.04
J1225+6109	−0.27	0.19	9.50	1.38E+38	21.26
J1253-0312	−0.71	0.23	9.11	1.07E+40	21.41
J1314+3452	−0.27	0.37	3.72	7.52E+37	20.71
J1359+5726	−0.27	0.19	6.34	1.66E+40	21.44
J1416+1223	−0.27	0.69	2.62	1.04E+41	20.19
J1418+2102	−0.27	0.11	1.17	1.92E+38	21.30
J1444+4237	−0.27	0.09	2.08	3.01E+37	21.57
J1448-0110	−0.37	0.28	4.08	6.91E+39	21.56
J1521+0759	0.52	0.42	3.52	7.86E+40	20.42
J1545+0858	−0.22	0.11	4.37	1.44E+40	21.54

a tracer of the neutral gas, we must correct for the fraction of the Si II found in the H II regions. Consequently, $\mathrm{ICF_{ion.}}$ has the net effect of reducing the inferred neutral-gas abundance of the affected species.

In order to obtain an accurate measure of $\mathrm{ICF_{neutral}}$ and $\mathrm{ICF_{ionized}}$, ad hoc photoionization models were made for each of the CLASSY galaxies using CLOUDY (G. J. Ferland et al. 2017). Simple spherical models were created using the metallicity of the source (Z), UV luminosity (L_{UV}), and H I column densities ($\log[N(\mathrm{H\,I})]$). Since the effective temperature (T_{eff}) of the stellar ionizing source was found to have a negligible effect on the ICF grids calculated by S. Hernandez et al. (2020), all models utilized a blackbody input spectrum fixed at $T_{\mathrm{eff}} = 4 \times 10^4$ K. Each model was initially run for a grid of hydrogen volume densities (n_{H}) with a range of $-3 < \log(n_{\mathrm{H}}/\mathrm{cm}^{-3}) < 3$. We then constrained the actual n_{H} value by comparing each model's level of ionization as a function of n_{H} against the galaxy's observed level of ionization of the neutral gas derived from $N(\mathrm{Fe\,III})/N(\mathrm{Fe\,II})$.

The ISM $\mathrm{Fe^{+2}/Fe^{+}}$ absorption-line ratio provides the cleanest way to measure the ionization state of the neutral gas due to the low oscillator strengths and multiple transitions involved.

When the ionization ratio was unobtainable for a galaxy (15 galaxies in total, mostly due to lack of coverage of Fe III λ1122), we utilized the average Fe III/Fe II ratio from the sample of Fe III/Fe II = –0.27. All model input parameters are given in Table 7.

The model of a given element was run twice, each with a different stopping criteria: (i) when the measured H I column density was reached (essentially the edge of the neutral cloud) and (ii) when the amount of ionized hydrogen was less than the neutral hydrogen (essentially the edge of the photodissociation region).

Since the models include neutral gas, cosmic rays are included in each run. The ICFs required for each element's column density within the neutral gas ($N(\mathrm{X})_{\mathrm{HI}}$) are then derived by sampling the column densities of the dominant neutral species $N(\mathrm{X}^i)$ and the more highly ionized species $N(\mathrm{X}^{i+1})$ from each of the two scenarios—first at the edge of the cloud ($N(\mathrm{X})_{\mathrm{HI+HII}}$) and second at the edge of the PDR ($N(\mathrm{X})_{\mathrm{HII}}$) such that:

$$N(\mathrm{X})_{\mathrm{HI}} = N(\mathrm{X})_{\mathrm{HI+HII}} - N(\mathrm{X})_{\mathrm{HII}}. \tag{A1}$$

We then obtained:

$$\mathrm{ICF_{ion.}} = \log[N(\mathrm{X}^i)_{\mathrm{HII}}] = \log[N(\mathrm{X}^i)_{\mathrm{HI+HII}}] - \log[N(\mathrm{X}^i)_{\mathrm{HI}}]\text{and:} \tag{A2}$$

$$\mathrm{ICF}(\mathrm{X}^i)_{\mathrm{neu.}} = \log[\frac{N(\mathrm{X}^i_{\mathrm{HI}}) + N(\mathrm{X}^{i+1}_{\mathrm{HI}})}{N(\mathrm{X}^i_{\mathrm{HI}})}]. \tag{A3}$$

The total ICF can then be defined as:

$$\begin{gathered}\mathrm{ICF_{tot.}} = \mathrm{ICF_{neu.}} - \mathrm{ICF_{ion.}}\\ \log[\mathrm{N(X)_{ICF}}] = \log[\mathrm{N(X)}] + \mathrm{ICF_{tot.}}\end{gathered} \tag{A4}$$

where $\log[N(\mathrm{X})]$ corresponds to the measured column density of element X (see e.g. Table 8).

We present the individual ICF components, $\mathrm{ICF_{neu.}}$, $\mathrm{ICF_{ion.}}$, and $\mathrm{ICF_{tot.}}$ color-coded by $N(\mathrm{H\,I})$, UV luminosity (L_{UV}), metallicity, and ionization factor (Fe III/Fe II) in Figures 14–16 , according to the input parameters shown in Table 7. As can be seen in Figure 14, $\mathrm{ICF_{neu.}}$ are sensitive to all four parameters within the spherical model, with larger values (i.e., larger amounts of higher-ionization gas to account for) accompanying models with higher metallicities, higher luminosities, and lower H I column densities. There is a weaker dependence of $\mathrm{ICF_{neu.}}$ on the ionization fraction utilized. For $\mathrm{ICF_{ion.}}$, there is a similar dependency in that the corrections for the amount of the neutral gas' dominant ion in the ionized gas are the largest at high metallicities, high luminosities, and low H I column densities (as can be seen in Figure 15).

Table 8

Column Density Measurements (Logarithmic, in Units of cm^{-2}) and b-parameters (in Units of km s^{-1})

Target	z	N(HI)	N(N I)	*b*	N(O I)	*b*	N(P II)	*b*	N(S II)	*b*	N(Fe II)	*b*	N(Fe III)	*b*
J0127-0619	0.005	21.21 ± 0.27	15.50 ± 0.10	29.98 ± 15.50	> 15.24	23.67 ± 2.41	13.80 ± 0.10	29.69 ± 11.34	15.77 ± 0.05	40.59 ± 5.68	15.19 ± 0.11	27.53 ± 3.56	…	…
J0144+0453	0.005	20.18 ± 0.02	14.35 ± 0.09	55.90 ± N/A	> 16.05	55.90 ± 5.14	13.52 ± 0.20	55.90 ± N/A	15.22 ± 0.08	55.90 ± N/A	15.04 ± 0.22	14.97 ± 3.00	…	…
J0337-0502[a]	0.014	21.81 ± 0.004	14.83 ± 0.02	33.14 ± 2.84	> 14.92	13.13 ± 0.56	12.97 ± 0.15	30.87 ± 12.48	14.96 ± 0.03	34.49 ± 2.62	15.32 ± 0.04	42.10 ± 4.74	14.24 ± 0.07	41.43 ± 9.50
J0405-3648	0.003	20.80 ± 0.02	14.45 ± 0.38	40.63 ± 75.43	…	…	13.33 ± 0.11	24.89 ± N/A	14.90 ± 0.11	75.27 ± 54.13	14.89 ± 0.33	7.88 ± 4.66	…	…
J0823+2806	0.047	21.61 ± 0.03	> 15.80	74.06 ± 34.03	> 16.41	90.44 ± 8.44	…	…	16.03 ± 0.03	101.89 ± 7.65	15.80 ± 0.34	86.73 ± 32.39	14.69 ± 0.16	90.44 ± N/A
J0934+5514	0.003	21.24 ± 0.002	14.54 ± 0.06	33.49 ± 26.32	> 14.50	15.86 ± 2.08	13.25 ± 0.19	15.86 ± N/A	14.96 ± 0.05	15.86 ± N/A	14.81 ± 0.06	17.75 ± 1.23	14.96 ± 0.26	15.86 ± N/A
J0938+5428	0.102	20.34 ± 0.08	14.82 ± 0.04	75.15 ± 15.05	> 15.26	126.74 ± 8.05	13.85 ± 0.08	126.74 ± N/A	15.26 ± 0.07	126.74 ± N/A	14.73 ± 0.11	126.74 ± N/A	…	…
J0940+2935	0.002	21.26 ± 0.01	14.72 ± 0.05	58.84 ± N/A	…	…	13.60 ± 0.12	58.87 ± N/A	15.38 ± 0.38	12.51 ± 10.31	15.42 ± 0.41	13.89 ± 3.27	…	…
J0944-0038	0.005	21.67 ± 0.05	15.29 ± 0.06	110.22 ± 32.70	> 15.49	53.23 ± 16.00	14.52 ± 0.09	135.08 ± 42.21	15.45 ± 0.20	53.23 ± N/A	15.81 ± 0.38	29.94 ± 6.51	…	…
J0944+3442	0.020	21.51 ± 0.03	15.11 ± 0.05	75.81 ± N/A	> 15.83	75.81 ± 11.52	13.92 ± 0.13	75.81 ± N/A	…	…	14.73 ± 0.21	71.70 ± 11.97	15.38 ± 0.08	82.39 ± 13.12
J1024+0524	0.033	20.58 ± 0.07	14.32 ± 0.07	106.93 ± N/A	> 15.64	106.93 ± 19.41	> 13.57	106.93 ± N/A	15.16 ± 0.06	129.61 ± 25.84	14.78 ± 0.20	109.99 ± 67.19	14.89 ± 0.03	157.53 ± 12.40
J1025+3622	0.127	20.69 ± 0.19	14.34 ± 0.13	106.46 ± N/A	> 15.84	106.46 ± 9.23	…	…	15.26 ± 0.09	106.46 ± N/A	15.55 ± 0.13	106.46 ± N/A	14.57 ± 0.17	88.50 ± 30.91
J1044+0353	0.013	21.84 ± 0.03	15.47 ± 0.32	15.32 ± 4.56	> 15.21	22.97 ± 2.78	13.85 ± 0.08	76.56 ± 18.01	15.47 ± 0.04	39.09 ± 5.55	15.58 ± 0.09	21.33 ± 1.44	14.35 ± 0.12	22.97 ± N/A
J1105+4444	0.022	21.87 ± 0.07	15.39 ± 0.03	85.17 ± 16.74	> 15.74	110.33 ± 3.62	14.10 ± 0.05	77.98 ± 22.25	15.93 ± 0.04	65.23 ± 7.77	15.73 ± 0.11	46.42 ± 5.40	15.00 ± 0.06	143.41 ± 62.79
J1119+5130	0.004	20.77 ± 0.03	14.22 ± 0.10	56.88 ± N/A	> 16.07	56.88 ± 8.92	13.38 ± 0.15	56.88 ± N/A	15.19 ± 0.11	56.88 ± N/A	15.64 ± 0.49	7.05 ± 2.19	…	…
J1129+2034	0.005	21.11 ± 0.01	15.48 ± 0.09	33.07 ± 3.78	> 15.78	59.10 ± 14.27	13.82 ± 0.09	56.32 ± 19.70	15.74 ± 0.09	36.30 ± 12.34	15.27 ± 0.10	26.99 ± 3.20	…	…
J1132+5722	0.005	21.24 ± 0.02	14.78 ± 0.05	64.90 ± N/A	> 15.93	64.98 ± 4.55	13.25 ± 0.21	50.68 ± 53.01	15.28 ± 0.08	64.90 ± N/A	14.92 ± 0.08	64.90 ± N/A	…	…
J1132+1411	0.018	20.53 ± 0.01	15.17 ± 0.03	94.65 ± 17.09	> 14.74	44.94 ± 14.24	13.74 ± 0.11	44.94 ± N/A	15.98 ± 0.09	44.94 ± N/A	15.28 ± 0.07	49.86 ± 4.48	15.12 ± 0.07	205.51 ± 42.01
J1144+4012	0.127	20.52 ± 0.06	15.08 ± 0.09	117.71 ± 49.22	> 16.39	160.95 ± 6.14	…	…	15.55 ± 0.07	124.44 ± 23.85	15.64 ± 0.35	88.14 ± 54.56	14.99 ± 0.07	104.82 ± 22.65
J1148+2546	0.045	21.19 ± 0.03	14.87 ± 0.03	53.27 ± 8.77	> 16.51	63.45 ± 5.90	13.91 ± 0.09	126.75 ± 33.00	15.45 ± 0.03	63.45 ± N/A	15.62 ± 0.07	63.45 ± N/A	14.88 ± 0.08	140.63 ± 26.07
J1150+1501	0.002	21.04 ± 0.01	15.45 ± 0.26	22.27 ± 5.42	> 15.46	46.97 ± 4.18	13.67 ± 0.14	46.93 ± N/A	15.52 ± 0.04	46.93 ± N/A	14.90 ± 0.12	33.80 ± 6.28	…	…
J1225+6109	0.002	21.26 ± 0.01	15.32 ± 0.14	21.03 ± 3.41	…	…	13.64 ± 0.14	23.25 ± N/A	15.43 ± 0.05	40.40 ± 11.28	15.18 ± 0.12	20.72 ± 2.33	…	…
J1253-0312	0.023	21.41 ± 0.04	15.78 ± 0.12	9.85 ± 5.24	> 14.89	62.26 ± 19.72	13.68 ± 0.06	53.45 ± 18.31	…	…	15.60 ± 0.18	15.81 ± 2.00	14.89 ± 0.03	70.36 ± 8.41
J1314+3452	0.003	20.71 ± 0.01	15.17 ± 0.37	11.12 ± 3.46	> 15.70	45.47 ± 4.70	13.72 ± 0.05	45.46 ± N/A	15.45 ± 0.06	23.83 ± 6.20	14.78 ± 0.06	45.23 ± 6.07	…	…
J1359+5726	0.034	21.44 ± 0.15	…	…	> 15.68	126.12 ± 3.25	13.48 ± 0.14	29.37 ± 37.18	15.22 ± 0.07	71.38 ± 22.98	14.89 ± 0.23	16.83 ± 3.99	…	…
J1416+1223	0.123	20.19 ± 0.05	15.47 ± 0.34	2.88 ± 3.47	> 15.95	262.30 ± 7.71	< 13.20	262.30 ± N/A	15.29 ± 0.08	111.89 ± 29.37	15.30 ± 0.20	83.01 ± 59.15	…	…
J1418+2102	0.009	21.30 ± 0.03	14.85 ± 0.04	38.22 ± 6.07	> 15.32	29.58 ± 6.75	13.34 ± 0.10	29.00 ± N/A	15.27 ± 0.05	28.32 ± 6.74	15.15 ± 0.18	15.15 ± 2.71	…	…
J1444+4237	0.002	21.57 ± 0.01	14.89 ± 0.06	33.51 ± 10.58	> 14.40	11.40 ± 3.06	13.38 ± 0.20	17.11 ± 51.11	15.63 ± 0.18	11.40 ± N/A	15.51 ± 0.72	9.54 ± 3.27	…	…
J1448-0110	0.027	21.56 ± 0.01	15.40 ± 0.35	16.62 ± 5.19	> 15.72	56.12 ± 6.55	13.74 ± 0.17	56.12 ± N/A	15.57 ± 0.04	47.05 ± 5.19	15.44 ± 0.08	32.34 ± 2.86	15.07 ± 0.04	119.11 ± 9.05
J1521+0759	0.094	20.42 ± 0.11	14.48 ± 0.80	5.00 ± 0.00	> 16.03	112.87 ± N/A	13.57 ± 0.13	112.87 ± N/A	…	…	14.47 ± 0.04	112.80 ± N/A	14.99 ± 0.04	118.49 ± 17.51
J1545+0858	0.038	21.54 ± 0.04	14.69 ± 0.05	65.87 ± N/A	> 15.57	65.87 ± 8.44	13.54 ± 0.40	20.12 ± 41.17	…	…	14.97 ± 0.10	73.59 ± 25.10	14.75 ± 0.05	94.45 ± 13.75

Notes. Uncertainties on *b*-parameters denoted as N/A correspond to cases where best fits were found by fixing the *b*-parameters to those derived by (Paper XI). Lines known to be saturated are shown as lower limits.

[a] Measurements taken from B. L. James et al. (2014).

Table 9
Total ICFs Applied to the Neutral Gas Column Densities

Target	Nitrogen	Oxygen	Phosphorus	Sulfur	Iron
J0127-0619	2.42E-02	1.80E-02	−2.45E-02	−8.19E-03	−3.33E-04
J0144+0453	1.29E-01	1.24E-01	−2.47E-01	−4.68E-02	8.56E-02
J0337-0502	3.41E-02	2.43E-02	−1.43E-02	−3.14E-03	1.28E-03
J0405-3648	2.15E-02	1.67E-02	−7.57E-02	−2.77E-02	−6.56E-04
J0823+2806	1.77E-02	1.70E-02	−2.29E-02	−7.21E-03	−1.70E-03
J0934+5514	1.92E-02	1.43E-02	−4.70E-02	−1.44E-02	−3.98E-04
J0938+5428	2.18E-01	2.00E-01	−1.80E-01	3.86E-02	1.49E-01
J0940+2935	2.69E-02	1.99E-02	−2.05E-02	−7.99E-03	−4.65E-04
J0944-0038	3.58E-02	2.60E-02	−9.88E-03	−2.62E-03	1.13E-03
J0944+3442	1.98E-02	1.51E-02	−2.45E-02	−7.76E-03	−3.13E-04
J1024+0524	9.38E-02	8.85E-02	−1.72E-01	−9.92E-03	6.77E-02
J1025+3622	3.53E-02	3.29E-02	−1.71E-01	−4.26E-02	1.22E-02
J1044+0353	4.18E-02	2.95E-02	−9.76E-03	−1.71E-03	2.06E-03
J1105+4444	3.33E-02	2.57E-02	−9.19E-03	−1.87E-03	7.30E-04
J1119+5130	2.17E-02	1.84E-02	−1.07E-01	−3.56E-02	1.04E-03
J1129+2034	9.36E-03	1.31E-02	−4.03E-02	−1.60E-02	−4.77E-03
J1132+5722	2.13E-02	1.58E-02	−3.75E-02	−1.34E-02	−9.54E-04
J1132+1411	4.39E-02	4.18E-02	−1.78E-01	−4.95E-02	1.28E-02
J1144+4012	7.37E-02	6.69E-02	−1.94E-01	−2.98E-02	3.09E-02
J1148+2546	1.35E-02	1.28E-02	−6.26E-02	−2.00E-02	−2.77E-03
J1150+1501	1.11E-02	1.29E-02	−5.47E-02	−2.04E-02	−4.31E-03
J1225+6109	2.05E-02	1.64E-02	−3.15E-02	−1.17E-02	−1.78E-03
J1253-0312	1.60E-02	1.40E-02	−3.64E-02	−1.21E-02	−2.14E-03
J1314+3452	1.05E-02	1.19E-02	−9.82E-02	−3.87E-02	−6.40E-03
J1359+5726	1.52E-02	1.31E-02	−3.54E-02	−1.02E-02	−1.48E-03
J1416+1223	3.48E-01	3.23E-01	−1.38E-01	1.05E-01	2.34E-01
J1418+2102	2.18E-02	1.65E-02	−3.23E-02	−1.11E-02	−9.27E-04
J1444+4237	3.49E-02	2.51E-02	−1.12E-02	−3.36E-03	1.06E-03
J1448-0110	1.76E-02	1.56E-02	−2.46E-02	−7.50E-03	−1.36E-03
J1521+0759	2.34E-01	2.15E-01	−1.31E-01	9.05E-02	1.65E-01
J1545+0858	1.84E-02	1.42E-02	−3.07E-02	−9.47E-03	−6.41E-04

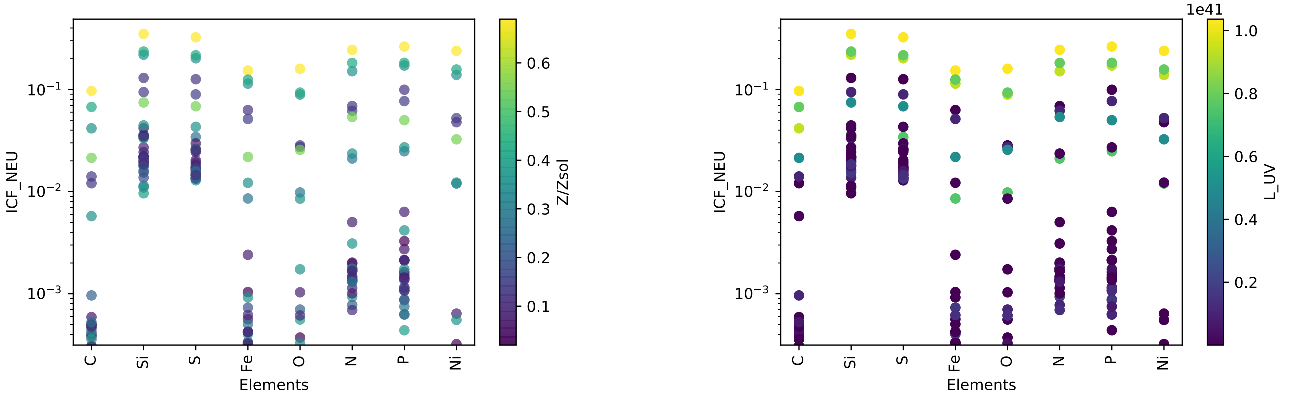

(a) ICF$_{\rm neutral}$ vs. metallicity **(b) ICF$_{\rm neutral}$ vs. L_{UV}**

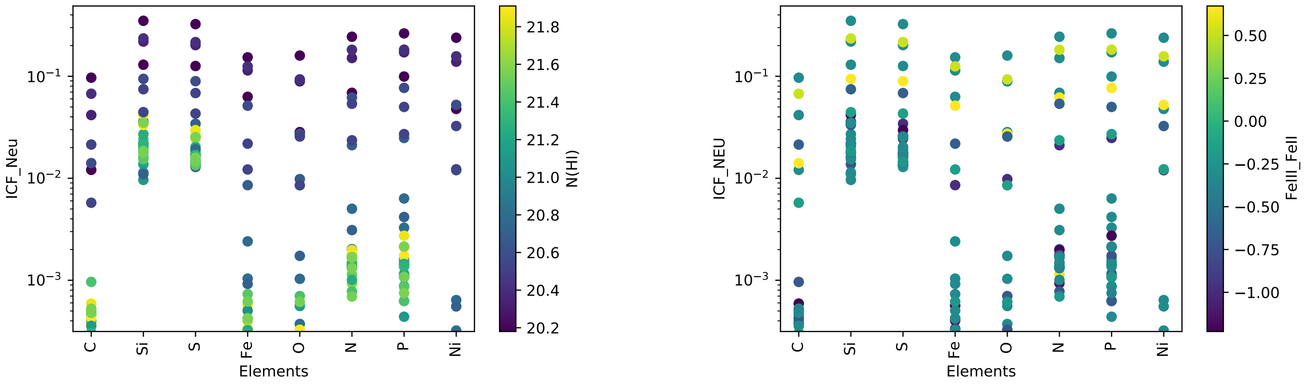

(c) ICF$_{\rm neutral}$ vs. N(H I) **(d) ICF$_{\rm neutral}$ vs. ionization factor**

Figure 14. ICF$_{\rm neutral}$ for each species, color-coded by the Cloudy model input parameters shown in Table 7, as described in Appendix A.

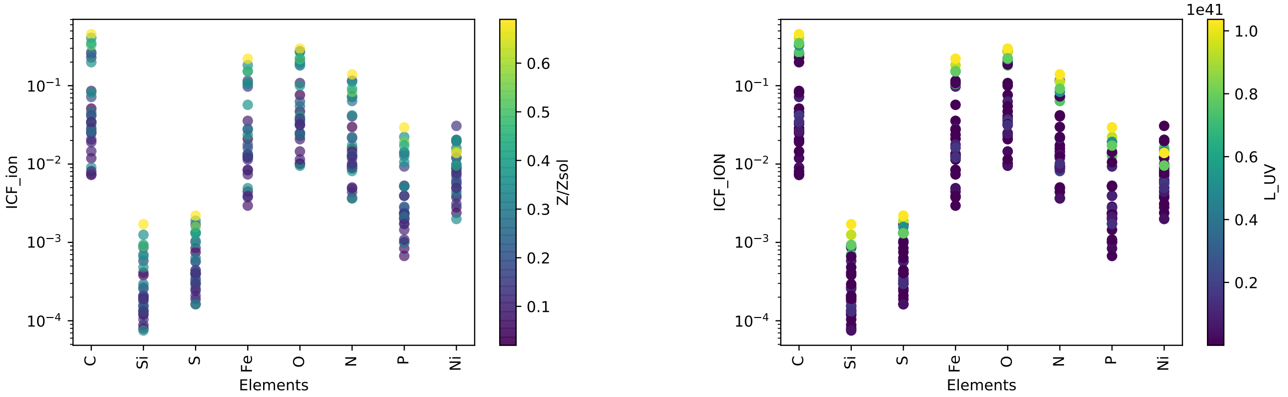

(a) $\mathrm{ICF}_{\mathrm{ionized}}$ vs. metallicity **(b) $\mathrm{ICF}_{\mathrm{ionized}}$ vs. L_{UV}**

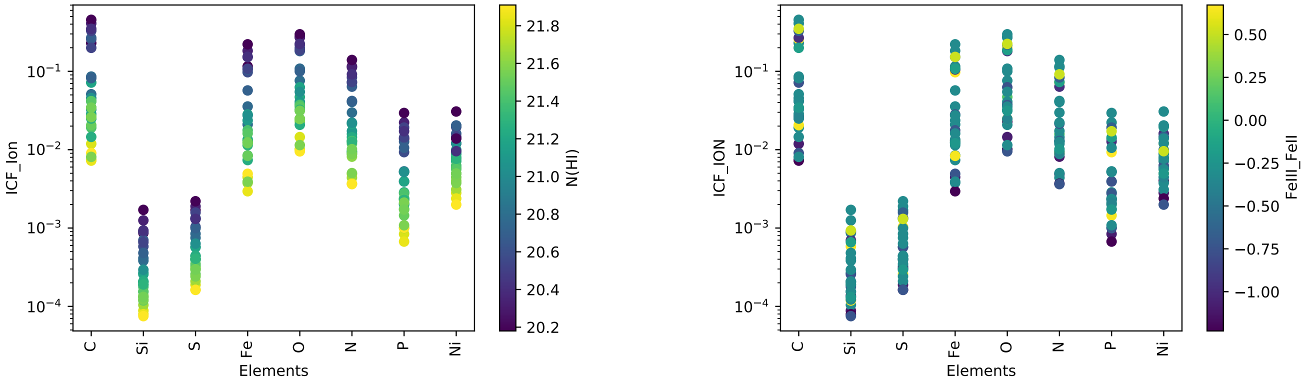

(c) $\mathrm{ICF}_{\mathrm{ionized}}$ vs. $N(\mathrm{H\,I})$ **(d) $\mathrm{ICF}_{\mathrm{ionized}}$ vs. ionization factor**

Figure 15. $\mathrm{ICF}_{\mathrm{ionized}}$ for each species, color-coded by the Cloudy model input parameters shown in Table 7, as described in Appendix A.

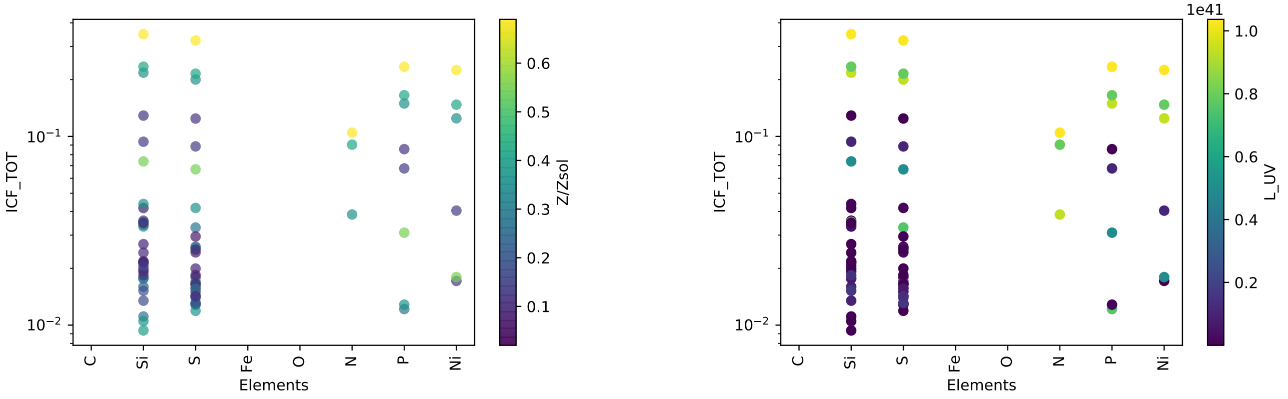

(a) $\mathbf{ICF}_{\text{total}}$ vs. metallicity

(b) $\mathbf{ICF}_{\text{total}}$ vs. L_{UV}

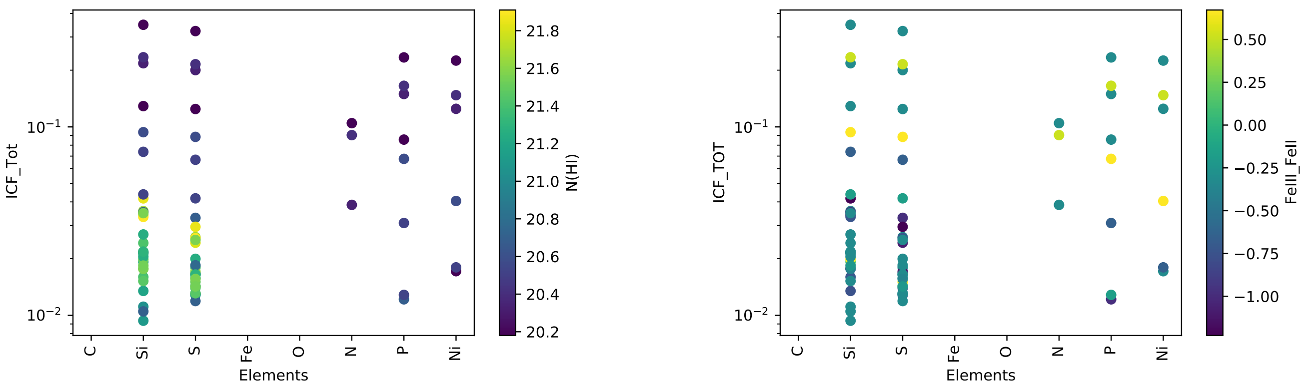

(c) $\mathbf{ICF}_{\text{total}}$ vs. $N(\mathbf{H}\,\textsc{i})$

(d) $\mathbf{ICF}_{\text{total}}$ vs. ionization factor

Figure 16. $\mathrm{ICF}_{\text{total}}$ for each species, color-coded by the Cloudy model input parameters shown in Table 7, as described in Appendix A.

Appendix B
Stellar Population Ages

Two sets of stellar population ages for the CLASSY galaxies were provided in Paper IV, both obtained via UV continuum fitting using simple stellar population models. These ages correspond to the median age of the best-fitting model, weighted by the fraction of contributed light to that model (i.e., the light-weighted UV-based stellar population age, $\mathrm{age}_{\mathrm{UV},L}$). As such, the resultant ages (ranging from ∼1 to 21 Myr, with a mean of 8 ± 5 Myr) represent the most recent burst of star formation and thus provide only limited temporal information regarding chemical mixing on short timescales. In order to sample longer chemical-evolutionary timescales sampled by our data, we instead use the mass-weighted ages ($\mathrm{age}_{\mathrm{UV},M}$)), which range from ∼1–36 Myr with a mean of 15 ± 12 Myr, that also sample the older, more-massive stellar populations.

For comparison, we additionally compute the mass-weighted ages derived from fitting the optical continuum, $\mathrm{age}_{\mathrm{opt},L}$, as detailed in Paper IV and Paper V. These instead sample *only* the older stellar populations in each system and range from ∼24 Myr to ∼12 Gyr with a mean of $\sim 6 \pm 3$ Gyr. The methodology used to derive the optical-based ages is described in the following paragraphs. We provide all of the stellar population ages in Table 10.

Optical stellar continuum fits were performed with STARLIGHT20, a stellar population synthesis (SPS) code developed by I. F. Fernandes et al. (2005) to analyze optical spectroscopic data, using the stellar models of G. Bruzual & S. Charlot (2003), the extinction law of J. A. Cardelli et al. (1989), and the IMF of G. Chabrier (2003), with 25 stellar ages ranging between 1 Myr and 18 Gyr. We utilize the results of these optical fits to provide a comparison with the stellar population ages derived from SPS fitting to the UV stellar continuum (also described in Paper IV) because the optical continuum samples the older stellar populations and can thus sample much longer enrichment timescales.

In order to derive the optical stellar population ages, we use the STARLIGHT outputs of the SPS models on the optical spectra in hand for our sample (SDSS, MUSE, MMT, KCWI, and VIMOS spectra). STARLIGHT uses a combination of spectral empirical evolution models of N simple stellar populations to fit the stellar continuum of an observed spectrum (O_λ). The emission lines, bad pixels, and sky residuals are masked during the fitting. For the CLASSY optical sample, we use a combination of $N = 150$ simple stellar populations, each characterized by different combinations of ages and metallicities, to model each of the O_λ. In order to get the best model spectrum (M_λ), STARLIGHT employs a combination of simulated annealing and a Metropolis scheme. This minimization performs successive explorations of the parameter space, geometrically increasing the light weights (x_j) of the different stellar populations until it gets a minimum χ^2 error/residual between O_λ and M_λ spectra along the

Table 10
Mass- and Light-weighted Ages of the Stellar Populations Derived from UV and Optical Spectra

	UV		Optical	
Target	log(Age/Myr)$_M$	log(Age/Myr)$_L$	log(Age/Gyr)$_M$	log(Age/Gyr)$_L$
J0127-0619	1.81 ± 0.33	1.90 ± 0.33	5.62 ± 0.40	0.64 ± 0.06
J0144+0453	8.95 ± 1.19	7.05 ± 0.88	0.34 ± 0.05	0.12 ± 0.02
J0337-0502	16.56 ± 2.49	5.74 ± 0.57	10.36 ± 0.72	1.45 ± 0.11
J0405-3648	36.11 ± 5.96	21.37 ± 3.36	0.89 ± 0.10	0.29 ± 0.03
J0823+2806	23.31 ± 3.81	6.87 ± 1.02	13.28 ± 0.83	1.41 ± 0.09
J0934+5514	28.18 ± 4.59	13.48 ± 2.01	0.08 ± 0.01	0.04 ± 0.01
J0938+5428	6.93 ± 0.74	5.79 ± 0.64	9.41 ± 0.68	0.46 ± 0.03
J0940+2935	31.95 ± 5.25	15.57 ± 2.41	4.63 ± 0.50	0.58 ± 0.07
J0944+3442	32.29 ± 5.33	14.06 ± 2.18	6.34 ± 0.49	1.03 ± 0.09
J0944-0038	34.23 ± 5.70	13.51 ± 2.18	12.44 ± 0.70	1.38 ± 0.08
J1024+0524	5.65 ± 0.66	4.91 ± 0.54	12.71 ± 0.75	1.06 ± 0.07
J1025+3622	7.71 ± 0.93	6.82 ± 0.83	14.03 ± 0.88	1.21 ± 0.08
J1044+0353	32.22 ± 5.33	10.62 ± 1.58	12.92 ± 0.88	1.31 ± 0.09
J1105+4444	26.39 ± 4.41	7.41 ± 1.27	6.22 ± 0.48	0.75 ± 0.06
J1119+5130	27.05 ± 4.38	12.64 ± 1.83	14.30 ± 0.77	1.35 ± 0.07
J1129+2034	3.14 ± 0.42	2.56 ± 0.36	12.45 ± 0.76	1.74 ± 0.12
J1132+1411	12.24 ± 1.37	8.20 ± 0.93	5.94 ± 0.54	0.73 ± 0.07
J1132+5722	18.50 ± 1.56	13.85 ± 1.22	14.88 ± 0.83	0.89 ± 0.05
J1144+4012	13.09 ± 1.36	10.84 ± 1.10	7.42 ± 0.65	0.74 ± 0.07
J1148+2546	6.85 ± 0.84	5.75 ± 0.70	12.69 ± 0.77	1.39 ± 0.09
J1150+1501	17.38 ± 2.71	6.44 ± 0.81	11.08 ± 0.77	0.83 ± 0.06
J1225+6109	23.51 ± 3.82	6.96 ± 0.95	0.56 ± 0.07	0.09 ± 0.01
J1253-0312	3.73 ± 0.33	3.75 ± 0.33	11.46 ± 0.76	1.25 ± 0.09
J1314+3452	2.25 ± 0.33	2.31 ± 0.33	9.65 ± 0.70	1.35 ± 0.10
J1359+5726	34.55 ± 5.72	14.59 ± 2.25	13.62 ± 0.86	1.73 ± 0.11
J1416+1223	7.80 ± 0.56	6.06 ± 0.47	2.13 ± 0.27	0.16 ± 0.02
J1418+2102	1.55 ± 0.33	1.64 ± 0.33	13.68 ± 0.61	0.54 ± 0.03
J1444+4237	34.69 ± 5.74	15.44 ± 2.36	8.96 ± 0.52	0.52 ± 0.04
J1448-0110	3.00 ± 0.33	3.10 ± 0.33	8.20 ± 0.54	0.78 ± 0.06
J1521+0759	9.30 ± 0.68	8.46 ± 0.64	11.47 ± 0.78	0.91 ± 0.07
J1545+0858	3.47 ± 0.33	3.55 ± 0.33	13.73 ± 0.78	1.32 ± 0.08

wavelength range. As a refinement stage, the complete loop is re-executed discarding populations with $x_j = 0$.

We use the individual STARLIGHT outputs containing the statistical light (x_j) and mass (m_j) weights of the used stellar populations, which represent the light and mass contribution of each population to the final best spectral model. The m_j values correspond to the current mass fraction of each stellar population at the end of the modeling run. The stellar ages and metallicities can be computed as the light-weighted or mass-weighted average contribution of all of the stellar populations used in the best model, as follows:

$$S = \sum_{j}^{N} S_j \times W_j, \tag{B1}$$

where S corresponds to the age or metallicity weighted average, S_j corresponds to the age or metallicity of each stellar population, and N is the number of stellar populations used. W_j is the light (W_{Lj}) or mass (W_{Mj}) fraction of the stellar populations with the same age (a), defined as:

$$W_j = \frac{\sum_j^N c_j[a]}{\sum_j^N c_j}, \tag{B2}$$

where c_j corresponds to x_j or m_j, to compute the light- and mass-weighted ages, respectively.

ORCID iDs

Bethan L. James https://orcid.org/0000-0003-4372-2006
Valentina Abril-Melgarejo https://orcid.org/0000-0002-2764-6069
Karla Z. Arellano-Córdova https://orcid.org/0000-0002-2644-3518
Adarsh Ranjan https://orcid.org/0000-0001-9882-1576
Kaelee S. Parker https://orcid.org/0000-0002-8809-4608
Danielle A. Berg https://orcid.org/0000-0002-4153-053X
Matilde Mingozzi https://orcid.org/0000-0003-2589-762X
Alessandra Aloisi https://orcid.org/0000-0003-4137-882X
John Chisholm https://orcid.org/0000-0002-0302-2577
Timothy Heckman https://orcid.org/0000-0001-6670-6370
Alaina Henry https://orcid.org/0000-0002-6586-4446
Svea Hernandez https://orcid.org/0000-0003-4857-8699
Kristen B. W. McQuinn https://orcid.org/0000-0001-5538-2614
Xinfeng Xu https://orcid.org/0000-0002-9217-7051
Chiaki Kobayashi https://orcid.org/0000-0002-4343-0487

References

Abril-Melgarejo, V., James, B. L., Aloisi, A., et al. 2024, ApJ, 973, 173
Arabsalmani, M., Garratt-Smithson, L., Wijers, N., et al. 2023, ApJ, 952, 67
Arellano-Córdova, K. Z., Mingozzi, M., Berg, D. A., et al. 2022, ApJ, 935, 74
Arellano-Córdova, K. Z., Berg, D. A., Mingozzi, M., et al. 2024, ApJ, 968, 98
Arellano-Córdova, K. Z., Berg, D. A., Mingozzi, M., et al. 2025, MNRAS, 544, 1588

Asplund, M., Amarsi, A. M., & Grevesse, N. 2021, A&A, 653, A141
Atek, H., Labbé, I., Furtak, L. J., et al. 2024, Natur, 626, 975
Berg, D. A., Chisholm, J., Erb, D. K., et al. 2021, ApJ, 922, 170
Berg, D. A., Erb, D. K., Henry, R. B. C., Skillman, E. D., & McQuinn, K. B. W. 2019, ApJ, 874, 93
Berg, D. A., James, B. L., King, T., et al. 2022, ApJS, 261, 31
Bland-Hawthorn, J., & Gerhard, O. 2016, ARA&A, 54, 529
Bruzual, G., & Charlot, S. 2003, MNRAS, 344, 1000
Bunker, A. J., Saxena, A., Cameron, A. J., et al. 2023, A&A, 677, A88
Cameron, A. J., Katz, H., Rey, M. P., & Saxena, A. 2023, MNRAS, 523, 3516
Cappellari, M., Scott, N., Alatalo, K., et al. 2013, MNRAS, 432, 1709
Cardelli, J. A., Clayton, G. C., & Mathis, J. S. 1989, ApJ, 345, 245
Carniani, S., Venturi, G., Parlanti, E., et al. 2024, A&A, 685, A99
Castellano, M., Napolitano, L., Fontana, A., et al. 2024, ApJ, 972, 143
Chabrier, G. 2003, PASP, 115, 763
Charbonnel, C., Schaerer, D., Prantzos, N., et al. 2023, A&A, 673, L7
Chisholm, J., Tremonti, C., & Leitherer, C. 2018, MNRAS, 481, 1690
Clark, I., Berg, D. A., Leitherer, C., Arellano-Córdova, K. Z., & Sander, A. A. C. 2024, ApJ, 964, 25
Crowther, P. A. 2007, ARA&A, 45, 177
De Cia, A., Jenkins, E. B., Fox, A. J., et al. 2021, Natur, 597, 206
De Cia, A., Ledoux, C., Mattsson, L., et al. 2016, A&A, 596, A97
De Cia, A., Ledoux, C., Petitjean, P., & Savaglio, S. 2018, A&A, 611, A76
De Cia, A., Roman-Duval, J., Konstantopoulou, C., et al. 2024, A&A, 683, A216
De Looze, I., Barlow, M. J., Swinyard, B. M., et al. 2017, MNRAS, 465, 3309
Edvardsson, B., Andersen, J., Gustafsson, B., et al. 1993, A&A, 275, 101
Emerick, A., Bryan, G. L., & Mac Low, M.-M. 2020, ApJ, 890, 155
Emerick, A., Bryan, G. L., Mac Low, M.-M., et al. 2018, ApJ, 869, 94
Ferland, G. J., Chatzikos, M., Guzmán, F., et al. 2017, RMxAA, 53, 385
Fernandes, I. F., Gruenwald, R., & Viegas, S. M. 2005, MNRAS, 364, 674
Finkelstein, S. L., Bagley, M. B., Arrabal Haro, P., et al. 2022, ApJL, 940, L55
Heckman, T. M., Alexandroff, R. M., Borthakur, S., Overzier, R., & Leitherer, C. 2015, ApJ, 809, 147
Henry, R. B. C., Edmunds, M. G., & Köppen, J. 2000, ApJ, 541, 660
Hernandez, S., Aloisi, A., James, B. L., et al. 2020, ApJ, 892, 19
Hernandez, S., Aloisi, A., James, B. L., et al. 2021, ApJ, 908, 226
Hibbert, A. 1988, PhyS, 38, 37
Hirai, Y., & Saitoh, T. R. 2017, ApJL, 838, L23
Hopkins, P. F., Grudić, M. Y., Wetzel, A., et al. 2019, MNRAS, 491, 3702
Howk, J. C., Sembach, K. R., Roth, K. C., & Kruk, J. W. 2000, ApJ, 544, 867
Hu, W., Martin, C. L., Gronke, M., et al. 2023, ApJ, 956, 39
Hunter, L. C., van Zee, L., McQuinn, K. B. W., Garner, R., & Dolphin, A. E. 2022, AJ, 163, 132
Izotov, Y. I., Stasińska, G., Meynet, G., Guseva, N. G., & Thuan, T. X. 2006, A&A, 448, 955
James, B., & Aloisi, A. 2018, ApJ, 853, 124
James, B. L., Aloisi, A., Heckman, T., Sohn, S. T., & Wolfe, M. A. 2014, ApJ, 795, 109
James, B. L., Kumari, N., Emerick, A., et al. 2020, MNRAS, 495, 2564
James, B. L., Tsamis, Y. G., Barlow, M. J., et al. 2009, MNRAS, 398, 2
James, B. L., Tsamis, Y. G., Walsh, J. R., Barlow, M. J., & Westmoquette, M. S. 2013, MNRAS, 430, 2097
James, B. L., Berg, D. A., King, T., et al. 2022, ApJS, 262, 37
Jecmen, M. C., & Oey, M. S. 2023, ApJ, 958, 149
Jenkins, E. B. 1986, ApJ, 304, 739
Jenkins, E. B. 2009, ApJ, 700, 1299
Kobayashi, C., & Ferrara, A. 2024, ApJL, 962, L6
Kobayashi, C., Karakas, A. I., & Lugaro, M. 2020, ApJ, 900, 179
Kobayashi, C., Karakas, A. I., & Umeda, H. 2011, MNRAS, 414, 3231
Kobayashi, C., Umeda, H., Nomoto, K., Tominaga, N., & Ohkubo, T. 2006, ApJ, 653, 1145
Konstantopoulou, C., De Cia, A., Krogager, J.-K., et al. 2022, A&A, 666, A12
Konstantopoulou, C., De Cia, A., Ledoux, C., et al. 2024, A&A, 681, A64
Krogager, J.-K. 2018, arXiv:1803.01187
Kumari, N., James, B. L., Irwin, M. J., Amorín, R., & Pérez-Montero, E. 2018, MNRAS, 476, 3793
Lagos, P., Telles, E., Nigoche Netro, A., & Carrasco, E. R. 2012, MNRAS, 427, 740
Le Fèvre, O., Tasca, L. A. M., Cassata, P., et al. 2015, A&A, 576, A79
Lebouteiller, V., Kunth, D., Thuan, T. X., & Désert, J. M. 2009, A&A, 494, 915
Leitherer, C., Schaerer, D., Goldader, J. D., et al. 1999, ApJS, 123, 3
Mac Low, M.-M., & Ferrara, A. 1999, ApJ, 513, 142
Maiolino, R., Scholtz, J., Witstok, J., et al. 2024, Natur, 630, E2
Majumder, S., Merlitz, H., Gopakumar, G., et al. 2002, ApJ, 574, 513
Mast, D., Rosales-Ortega, F. F., Sánchez, S. F., et al. 2014, A&A, 561, A129
Matsuura, M., Dwek, E., Meixner, M., et al. 2011, Sci, 333, 1258
Matteucci, F. 2012, Chemical Evolution of Galaxies (Springer)
Matteucci, F., & Brocato, E. 1990, ApJ, 365, 539
Matteucci, F., & Chiappini, C. 2005, PASA, 22, 49
Mattsson, L., De Cia, A., Andersen, A. C., & Petitjean, P. 2019, A&A, 624, A103
McLure, R. J., Pentericci, L., Cimatti, A., et al. 2018, MNRAS, 479, 25
McQuinn, K. B. W., Skillman, E. D., Dolphin, A., et al. 2015, ApJL, 815, L17
McWilliam, A. 1997, ARA&A, 35, 503
Méndez-Delgado, J. E., Kreckel, K., Esteban, C., et al. 2024, A&A, 690, A248
Mingozzi, M., James, B. L., Arellano-Córdova, K. Z., et al. 2022, ApJ, 939, 110
Mingozzi, M., James, B. L., Berg, D. A., et al. 2024, ApJ, 962, 95
Morton, D. C. 1991, ApJS, 77, 119
Morton, D. C. 2003, ApJS, 149, 205
Murray, N., Quataert, E., & Thompson, T. A. 2005, ApJ, 618, 569
Nandal, D., Regan, J. A., Woods, T. E., et al. 2024, A&A, 683, A156
Parker, K. S., Berg, D. A., Gazagnes, S., et al. 2024, ApJ, 977, 104
Peeples, M. S., & Shankar, F. 2011, MNRAS, 417, 2962
Pérez-Montero, E., Contini, T., Lamareille, F., et al. 2013, A&A, 549, A25
Prochaska, J. X. 2006, ApJ, 650, 272
Quinet, P. 1996, A&AS, 116, 573
Recchi, S., Spitoni, E., Matteucci, F., & Lanfranchi, G. A. 2008, A&A, 489, 555
Rivera-Thorsen, T. E., Chisholm, J., Welch, B., et al. 2024, A&A, 690, A269
Rodríguez, M. 1999, A&A, 348, 222
Rodríguez, M., & Rubin, R. H. 2005, ApJ, 626, 900
Schaerer, D., Marques-Chaves, R., Xiao, M., & Korber, D. 2024, A&A, 687, L11
Searle, L. 1971, ApJ, 168, 327
Senchyna, P., Plat, A., Stark, D. P., et al. 2024, ApJ, 966, 92
Senchyna, P., Stark, D. P., Charlot, S., et al. 2021, MNRAS, 503, 6112
Shapley, A. E., Reddy, N. A., Kriek, M., et al. 2015, ApJ, 801, 88
Simmonds, C., Tacchella, S., Hainline, K., et al. 2024, MNRAS, 527, 6139
Spitzer, L., Jr, & Fitzpatrick, E. L. 1993, ApJ, 409, 299
Steidel, C. C., Rudie, G. C., Strom, A. L., et al. 2014, ApJ, 795, 165
Tang, M., Stark, D. P., Chen, Z., et al. 2023, MNRAS, 526, 1657
Tayal, S. S. 1995, ApJ, 446, 895
Tinsley, B. M. 1979, ApJ, 229, 1046
Tolstoy, E., Hill, V., & Tosi, M. 2009, ARA&A, 47, 371
Topping, M. W., Stark, D. P., Senchyna, P., et al. 2024, MNRAS, 529, 3301
Tumlinson, J., Peeples, M. S., & Werk, J. K. 2017, ARA&A, 55, 389
van Zee, L., & Haynes, M. 2006, ApJ, 636, 214
Velichko, A., De Cia, A., Konstantopoulou, C., et al. 2024, A&A, 685, A103
Verner, D. A., Barthel, P. D., & Tytler, D. 1994, A&AS, 108, 287
Verner, D. A., Verner, E. M., & Ferland, G. J. 1996, ADNDT, 64, 1
Vink, J. S. 2025, IAUS, 19, 106
Westmoquette, M. S., James, B., Monreal-Ibero, A., & Walsh, J. R. 2013, A&A, 550, A88
Wiese, W. L., Fuhr, J. R., & Deters, T. M. (ed.) 1996, Atomic Transition Probabilities of Carbon, Nitrogen, and Oxygen : A Critical Data Compilation, Journal of Physical and Chemical Reference Data (AIP Press)
Wiseman, P., Schady, P., Bolmer, J., et al. 2017, A&A, 599, A24
Xu, X., Heckman, T., Henry, A., et al. 2022, ApJ, 933, 222
Xu, X., Henry, A., Heckman, T., et al. 2025, ApJ, 984, 94
Zaritsky, D., Kennicutt, J. C. R., & Huchra, J. 1994, ApJ, 420, 87
Zhang, H. 1996, A&AS, 119, 523
Zheng, Y., Faerman, Y., Oppenheimer, B. D., et al. 2024, ApJ, 960, 55
Zsargo, J., & Federman, S. R. 1998, ApJ, 498, 256